OUKA
Osaka University Knowledge Archive

Title	Sparsity-Aware OCT Volumetric Data Restoration Using Optical Synthesis Model
Author(s)	Kobayashi, Ruiki; Fujii, Genki; Yoshida, Yuta et al.
Citation	IEEE Transactions on Computational Imaging. 2022, 8, p. 505-520
Version Type	AM
URL	https://hdl.handle.net/11094/93363
rights	© 2022 IEEE. Personal use of this material is permitted. Permission from IEEE must be obtained for all other uses, in any current or future media, including reprinting/republishing this material for advertising or promotional purposes, creating new collective works, for resale or redistribution to servers or lists, or reuse of any copyrighted component of this work in other works.
Note	

Osaka University Knowledge Archive : OUKA

https://ir.library.osaka-u.ac.jp/

Osaka University

Sparsity-Aware OCT Volumetric Data Restoration Using Optical Synthesis Model

Ruiki Kobayashi, *Student, IEEE,* Genki Fujii, Yuta Yoshida, Takeru Ota, Fumiaki Nin, Hiroshi Hibino Samuel Choi, *Member, IEEE,* Shunsuke Ono, *Member, IEEE,* and Shogo Muramatsu, *Senior, IEEE,*

***Abstract*—In this study, a novel restoration model for the data of optical coherence tomography (OCT) is proposed. An OCT device acquires a tomographic image of a specimen at the scale of a few micrometers using a near-infrared laser and has been frequently adopted to measure the structures of bio-tissues. In certain applications, OCT devices face the problem of extremely weak reflected light and require the help of image processing to estimate the distribution of reflected light hidden in various noises. OCT identifies tomographic structures by searching for peak interference locations and their intensities. Therefore, the challenge of OCT data restoration involves the problem of identifying the interference function and its deconvolution. In this study, a restoration method is given by reducing the problem to a regularized least-squares problem with a hard constraint for the latent refractive index distributions, and an algorithm is derived using a primal-dual splitting (PDS) framework. The PDS has the advantage of requiring no inverse matrix operation and is able to handle high-dimensional data. The significance of the proposed method is verified through simulations using artificial data, followed by an experiment conducted using actual observation of $64 \times 64 \times 5000$ sized voxels.**

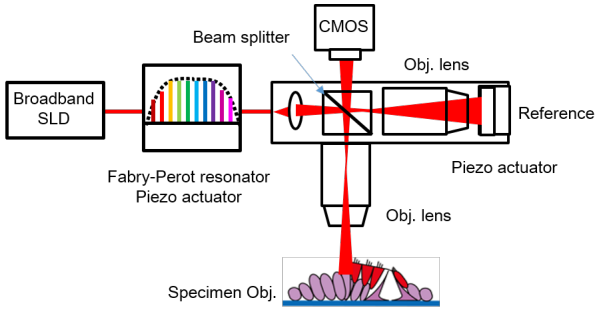

Fig. 1. The MS *en-face* OCT device uses a broadband super-luminescent diode (SLD) light source, where a Fabry-Perot resonator is used to generate a multi-wavelength optical comb. The interference peak position is scanned in the Z-direction by controlling the frequency interval of the spectrum comb with a piezo actuator. The optical comb is divided into reference and sample beams using a beam splitter. The field of view is enlarged by the objective lenses, and the reflected light is formed on the CMOS sensor. The interference between the reference and sample beams is acquired.

I. Introduction

Improvements in sensing technology used in extreme environments are indispensable for the development of science and medicine. In addition to hardware devices, physical models and signal-processing algorithms need to cooperate with each other. To measure the vibration of the sensory epithelium *in vivo* and contribute to the treatment of deafness, we are developing a multifrequency swept (MS) *en-face* optical coherence tomography (OCT) device that instantaneously captures the X-Y plane and acquires a tomographic image by optically scanning the Z-direction [1]. Fig. 1 briefly shows the configuration of the MS *en-face* OCT device.

OCT is a tomographic technique with a spatial resolution of a few micrometers using a near-infrared laser [2]. The structure of the target object is measured based on the interference between the reference light and the light reflected by the object. Typical OCT techniques, such as Doppler spectral domain (SD) OCT [3]–[6], acquire tomographic data in the Z-direction at a point on the X-Y plane and require mechanical 2-D scanning in the X- and Y-directions to construct 3-D volumetric data. Compared with other approaches, MS *en-face* OCT is able to observe a dynamic tomographic structure [7]. However, light is broadened by an interference microscope; hence, the light intensity of the image sensor becomes quite weak. As a result, the acquired interference is prone to hiding under severe noise. In [8], [9], Choi *et al.* adopted filtering in the FFT domain to extract high-energy spectral bands in the frequency domain through a manual operation to restore large-scale 3-D OCT data. However, an automated optimization is demanded to improve the efficiency and quality of the process.

The denoising of the OCT volumetric data is modeled as a signal restoration problem. In [10], we proposed a denoising method for OCT data using an iterative hard-thresholding algorithm. In [11], Cheng *et al.* proposed a method for solving OCT volumetric data restorations by modeling them as the sum of the underlying clean measurements and noise. In [12], Fang *et al.* proposed a super-resolution technique and speckle denoising method for retinal SD-OCT. In [13], Zaki *et al.*

This work was supported by JST [Moonshot R&D][Grant Number JPMJMS2024], AMED-CREST (Advanced Research and Development Programs for Medical Innovation) 22gm1510004 and 20gm0810004 from AMED, and JSPS KAKENHI Grant Numbers JP16H03164, JP18H04062, JP19H02151, JP19H04135, JP20K21883, JP20K20164, and JP22H00512.

R. Kobayashi (email: f20c050g@ieee.org), G. Fujii and Y. Yoshida were with Graduate School of Science and Technology, Niigata Univ., Niigata, Japan. S. Choi and S. Muramatsu (email: shogo@eng.niigata-u.ac.jp) are with the same school and AMED-CREST, AMED, Japan.

T. Ota and H. Hibino are with Division of Glocal Pharmacology, Department of Pharmacology, Graduate School of Medicine, Osaka University, Osaka, Japan and AMED-CREST, AMED, Japan.

F. Nin is with Department of Physiology, Division of Biological Principles, Graduate School of Medicine, Gifu University, Gifu, Japan and AMED-CREST, AMED, Japan.

S. Ono is with Laboratory for Future Interdisciplinary Research of Science and Technology, Institute of Innovative Research, Tokyo Institute of Technology, Kanagawa, Japan.

This paper has supplementary downloadable material available at http://ieeexplore.ieee.org, provided by the author. The material includes computer software (MATLAB code) to reproduce the figures and tables in this paper. This material is 3,152 kB in size.

demonstrated a noise adaptive wavelet thresholding algorithm that exploits the difference in noise characteristics in different wavelet sub-bands. In [14], Shamouilian *et al.* model speckle noise as a mixture of salt-and-pepper noise and additive white Gaussian noise (AWGN), and achieve speckle noise removal by preprocessing based on median filters and solving a Z-directional total variation (TV) regularized least squares problem. In addition, in [15], Hu *et al.* proposed a method of restoration using a variance-stabilizing transform called an Anscombe transform and 3-D Shearlets. However, none of these techniques considered the measurement process, that is, observation through interference. The restoration problem involves the removal of the measurement process as well as noise. Therefore, the identification of the coherence function must be considered.

In [16], we proposed a method based on the primal-dual plug-and-play (PDPnP) method [17] to restore the OCT data by considering the measurement process and the range of reflection ratio. PDPnP relies on the PDS algorithm [18], [19] and has an advantage of requiring no inverse matrix operations. Meanwhile, alternating direction method of multipliers (ADMM) [20], [21], which is a popular alternative to the PDS algorithm [22], works using a matrix inversion. Although the PDS requires a relatively large number of iterations, it is highly versatile and suitable for processing high-dimensional data, such as tomographic images. However, challenges remain in setting the reflectance constraints and spatial correlation of biological tissues in its application of the OCT restoration.

In this paper, we propose the introduction of a refractive index distribution into the model to obtain more sophisticated prior knowledge. The contributions of our study are summarized as follows:

a) Optical synthesis model: We provide a model that reflects the refractive index distribution of biological tissues as prior knowledge, which can be attributed to a convex optimization problem.

b) Measurement process model: We compensate the sampling interval to count for the non-linearity of the piezoelectric element, and then identify the coherence function as a convolutional kernel.

c) Algorithm: We develop a PDS-based algorhitm to solve a regularized least-squares problem with a hard constraint for the latent refractive index distributions, and use the PDS-based one to recover high-dimensional volumetric data.

Note that our proposed model is not limited to MS *en-face* OCT and can also be applied to other OCT configurations.

This paper reorganizes our previous study [23] by enhancing the derivation process of the algorithm and by focusing on the identification of the measurement process; theorems are extended, proofs are detailed, and performance evaluations are refined to consider the actual measurement process. We conduct parametric tuning to improve the observation model, which considers nonlinear characteristics owing to the piezoelectric element. It should be mentioned here that speckle denoising is a challenging issue for OCT. For the speckle noise removal, we adopt the model developed in the literature [14], which divides speckle denoising into salt-and-pepper denoising and regularized Gaussian denoising, the latter is mainly addressed in this paper, focusing on the effects of introducing an optical synthesis model.

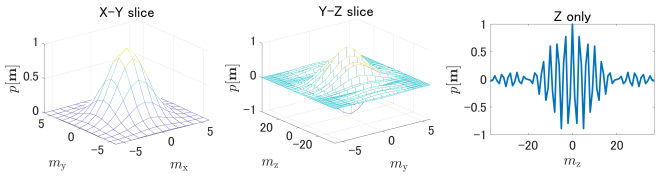

Fig. 2. Discrete model of coherence function defined by (2a), where the amplitude, X-Y axis standard deviation, Z-axis standard deviation, angular frequency, and scale factor are set to $\alpha_{\rm p}=1$, $\sigma_{\rm xy}=2$, $\sigma_{\rm z}=30$, $\omega_{\rm p}=0.3\pi$, and $b_{\rm p}=0.05$, respectively. (a) X-Y slice at the center of Z, (b) Y-Z slice at the center of X, and (c) Z only at the center of X and Y.

The remainder of this paper is organized as follows. Section II describes the OCT observation model and summarizes the challenges of OCT model restoration. Section III proposes a problem setting for OCT volumetric data restoration and to solve the problem yields an algorithm based on the PDS framework. Section IV evaluates the significance of the proposed method through artificial simulations, and Section V demonstrates experimental results with real observation data on the sensory epithelium of mouse, which were acquired through the MS *en-face* OCT. Finally, Section VI provides some concluding remarks regarding this research.

II. Review of the OCT Observation Model

In this section, we review the models of the OCT measurement process and noise. We then discuss the relationship between the synthesis model and the refractive-index distribution. In the following discussion, we assume that the light travels along the Z-axis.

A. Observation Model

OCT devices, in general, acquire tomographic images using the interference between the reference and the sample laser beam. A discrete model of the OCT observation data $\{t[\mathbf{n}]\}_{\mathbf{n}}\subset\mathbb{R}^{\Omega_{\rm v}}$ is modeled as follows:

$$t[\mathbf{n}]=b[\mathbf{n}]+\sum_{\mathbf{k}\in\Omega_{\rm r}}r[\mathbf{k}]p[\mathbf{n}-\mathbf{k}]+w[\mathbf{n}],\ \mathbf{n}\in\Omega_{\rm v},\quad(1)$$

where $\mathbf{n}=[n_{\rm x},n_{\rm y},n_{\rm z}]^{\intercal}\in\Omega_{\rm v}$ and $\mathbf{k}=[k_{\rm x},k_{\rm y},k_{\rm z}]^{\intercal}\in\Omega_{\rm r}$ are the array indexes of 3-D volumetric data. Each element corresponds to the position of the horizontal, vertical, and depth, respectively [24]. In addition, $\Omega_{\rm r},\Omega_{\rm v}\subset\mathbb{Z}^3$ represent the index domains[1]. In this paper, the superscript '$\intercal$' denotes the transposition. Here, $\{b[\mathbf{n}]\}_{\mathbf{n}}$ represents bias and trend component in the Z-direction that does not contribute to the interference. In addition, $\{w[\mathbf{n}]\}_{\mathbf{n}}$ denotes the noise component, which is assumed to be an additive; $\{p[\mathbf{m}]\}_{\mathbf{m}}$ is the interference waveform (i.e., the coherence function) representing the OCT measurement process; and $\{r[\mathbf{k}]\}_{\mathbf{k}}\subset\mathbb{R}^{\Omega_{\rm r}}$ corresponds to the reflectance distribution of the target object.

[1] $\Omega=\{0,1,\cdots,N_{\rm x}-1\}\times\{0,1,\cdots,N_{\rm y}-1\}\times\{0,1,\cdots,N_{\rm z}-1\}\subset\mathbb{Z}^3$ is an example of index domain. In this case, $\mathbb{R}^{\Omega}$ is also expressed by $\mathbb{R}^{N_{\rm x}\times N_{\rm y}\times N_{\rm z}}$ instead.

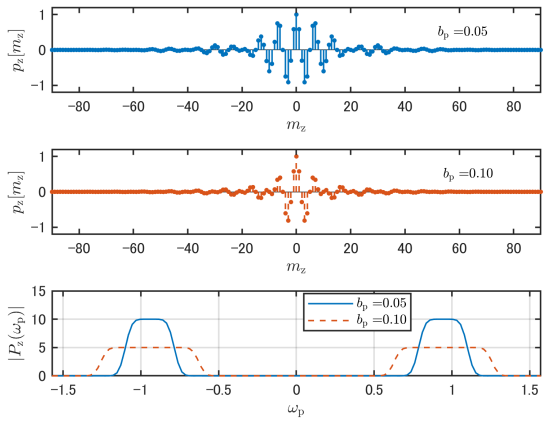

Fig. 3. Effect of the broadening factor b_p for $p_z[m_z]$ in (2c), where $|P_z(\omega_p)|$ is the amplitude frequency response of $p_z[\cdot]$, $\omega_p = 0.3\pi$ and $\sigma_z = 30$.

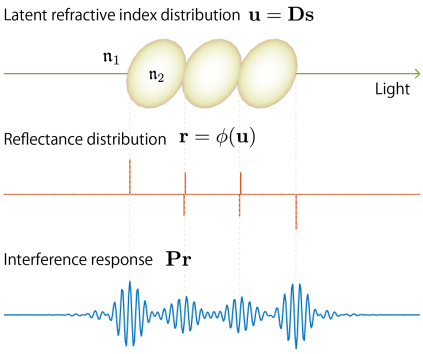

Fig. 4. Relationship among latent refractive index distribution $\mathbf{u}$, reflectance distribution $\mathbf{r}$ and interference response $\mathbf{Pr}$.

Fig. 2 shows an example of the coherence function $\{p[\mathbf{m}]\}_{\mathbf{m}}$. The coherence function has a spatial spread in the X-Y directions and a shape similar to the cosine modulated Gaussian function windowed by a sinc function in the Z-direction. The coherence function is modeled as follows:

$$p[\mathbf{m}] = \alpha_{\mathrm{p}} p_{\mathrm{xy}}[m_{\mathrm{x}}, m_{\mathrm{y}}] p_{\mathrm{z}}[m_{\mathrm{z}}], \ \mathbf{m} \in \mathbb{Z}^3, \tag{2a}$$

$$p_{\mathrm{xy}}[m_{\mathrm{x}}, m_{\mathrm{y}}] = \exp\left(-\frac{m_{\mathrm{x}}^2 + m_{\mathrm{y}}^2}{2\sigma_{\mathrm{xy}}^2}\right), \ m_{\mathrm{x}}, m_{\mathrm{y}} \in \mathbb{Z}, \tag{2b}$$

$$p_{\mathrm{z}}[m_{\mathrm{z}}] = \exp\left(-\frac{m_{\mathrm{z}}^2}{2\sigma_{\mathrm{z}}^2}\right) \cos\left(\omega_{\mathrm{p}} m_{\mathrm{z}}\right) \mathrm{sinc}(b_{\mathrm{p}} m_{\mathrm{z}}), \ m_{\mathrm{z}} \in \mathbb{Z}, \tag{2c}$$

where $\mathrm{sinc}(x)$ is defined as 1 for $\omega = 0$ and $\sin(\pi x)/\pi x$ for $\omega \neq 0$; $\mathbf{m} = [m_{\mathrm{x}}, m_{\mathrm{y}}, m_{\mathrm{z}}]^{\intercal}$; α_{p}, σ_{xy}, σ_{z}, ω_{p}, and b_{p} denote the amplitude, standard deviation in the X-Y plane, standard deviation along the Z-axis, angular frequency, and broadening factor, respectively. We define (2a) by generalizing a typical interference function model in two respects [24, §3.1.3]. In order to reflect the features of MS *en-face* OCT shown in Fig. 1, the first is to model the blurring in the X-Y plane with a 2-D Gaussian function in (2b), and the second is to model the broadband SLD features with the sinc function in the Z-direction. Fig. 3 illustrates the effect of the broadening factor b_p of (2c) in the frequency domain.

The reflectance distribution $\{r[\mathbf{k}]\}_{\mathbf{k}}$ is unknown and should be restored from the observation $\{t[\mathbf{n}]\}_{\mathbf{n}}$ by removing the bias $\{b[\mathbf{n}]\}_{\mathbf{n}}$, additive noise $\{w[\mathbf{n}]\}_{\mathbf{n}}$, and local oscillation through $\{p[\mathbf{m}]\}_{\mathbf{m}}$. Among these degradation factors, the bias component $\{b[\mathbf{n}]\}_{\mathbf{n}}$ can simply be removed using a high-pass filter because $\{b[\mathbf{n}]\}_{\mathbf{n}}$ is a constant or a ramp component with a slight slope in the Z-direction at each position in the X-Y plane, where the removal of bias $\{b[\mathbf{n}]\}_{\mathbf{n}}$ is achieved by subtracting a Z-directional moving average filtering result from the original $\{t[\mathbf{n}]\}_{\mathbf{n}}$. Thus, we adopted the following signal:

$$v[\mathbf{n}] = t[\mathbf{n}] - b[\mathbf{n}], \ \mathbf{n} \in \Omega_{\mathrm{v}} \tag{3}$$

as a restoration target.

B. Reflectance and Refractive Index

The reflectance is related to the refractive index. The reflection ratio R at the boundary of different refractive indices is obtained as follows:

$$R = \frac{|\mathfrak{n}_1 - \mathfrak{n}_2|(\mathfrak{n}_1 - \mathfrak{n}_2)}{(\mathfrak{n}_1 + \mathfrak{n}_2)^2}, \ \mathfrak{n}_1, \mathfrak{n}_2 \in [0, \infty), \tag{4}$$

where $\mathfrak{n}_1$ and $\mathfrak{n}_2$ are the refractive indices of the light incident and opposite sides, respectively. In (4), the phase shift is also considered, where the sign is determined based on their relationship. The refractive indices of the bio-tissues were assumed to have a spatial correlation and be within the range of approximately 1.00–1.50.

C. Challenges of OCT Volumetric Data Restoration

A restoration model is set to obtain the reflectance distribution $\{r[\mathbf{k}]\}_{\mathbf{k}}$ in (1) from the observation $\{v[\mathbf{n}]\}_{\mathbf{n}}$ in (3). This is an inverse problem. Although it appears to be simple, the inverse problem involves a large number of 3-D volumetric data. Consequently, the number of calculations and the memory consumption have become a serious problem. Therefore, an algorithm that does not use inverse matrices and consumes less memory is required. The following summarize some issues in the OCT volumetric data restoration.

- There is no method that reflects the refractive index distribution as prior knowledge.
- Owing to the non-linearity of the piezoelectric element, the sampling interval should be compensated.
- The algorithm should be applicable to high-dimensional volumetric data.

III. Proposed Restoration Model and Algorithm

We propose a novel model for restoring the reflectance distribution $\{r[\mathbf{k}]\}_{\mathbf{k}}$ from OCT observation data $\{v[\mathbf{n}]\}_{\mathbf{n}}$ by applying the relation to the latent refractive index distribution.

A. Observation Model of the OCT Device

We consider a latent refractive index distribution $\{u[\mathbf{k}]\}_{\mathbf{k}}$ as the source array for OCT observation $\{v[\mathbf{n}]\}_{\mathbf{n}}$. Now, let

$\mathbf{u} \triangleq \mathrm{vec}(\{u[\mathbf{k}]\}_{\mathbf{k}}) \in [a,b]^N \in \mathbb{R}^N$ $(0 < a < b < \infty)$, $\mathbf{r} \triangleq \mathrm{vec}(\{r[\mathbf{k}]\}_{\mathbf{k}}) \in \mathbb{R}^N$, $\mathbf{v} \triangleq \mathrm{vec}(\{v[\mathbf{n}]\}_{\mathbf{n}}) \in \mathbb{R}^M$, and $\mathbf{w} \triangleq \mathrm{vec}(\{w[\mathbf{n}]\}_{\mathbf{n}}) \in \mathbb{R}^M$, as the vector representations of the latent source, estimation target, observation, and noise, respectively, where $N = |\Omega_{\mathrm{r}}|$ and $M = |\Omega_{\mathrm{v}}|$. For these vector notations, a system with a coherence function $\{p[\mathbf{m}]\}_{\mathbf{m}}$ is represented by matrix $\mathbf{P} \in \mathbb{R}^{M\times N}$, where we temporarily assume a linear convolution. Fig. 4 shows the relationship between latent refractive index distribution $\mathbf{u}$, reflectance distribution $\mathbf{r}$ and interference response $\mathbf{Pr}$. From (1) and (3), the observation model is represented as

$$\mathbf{v} = \mathbf{P}\boldsymbol{\phi}(\mathbf{u}) + \mathbf{w}, \ \text{s.t.}\ \mathbf{u} \in [a,b]^N, \ a,b \in [0,\infty), \quad (5)$$

where $\mathbf{u}$ is the distribution of the latent refractive index, $[a,b]^N$ denotes the range of $\mathbf{u}$, and $\boldsymbol{\phi}\colon [0,\infty)^N \to (-1,1)^N$ maps the refractive index to that of the reflectance according to the relation in (4), that is, $\mathbf{r} = \boldsymbol{\phi}(\mathbf{u})$.

We can further assume the generation process of the latent distribution $\mathbf{u}$ using a synthesis dictionary $\mathbf{D} \in \mathbb{R}^{N\times L}$ and a coefficient vector $\mathbf{s} \in \mathbb{R}^L$ as

$$\mathbf{u} = \mathbf{D}\mathbf{s}. \quad (6)$$

As an advantage of this new model, hierarchical sparsity regularization can be applied to $\mathbf{r}$ and $\mathbf{s}$ with a hard constraint simultaneously placed on $\mathbf{u}$. Although it is not trivial to know the actual refractive index distribution, if the distribution has some spatial structure, the hypothetical distribution serves as an additional regularization.

From (4), a definition of $\boldsymbol{\phi}(\cdot)$ is given as

$$\boldsymbol{\phi}(\mathbf{u}) = \mathrm{abs}(\boldsymbol{\Delta}_{\mathrm{z}}\mathbf{u}) \odot (-\boldsymbol{\Delta}_{\mathrm{z}}\mathbf{u}) \oslash (\mathbf{A}_{\mathrm{z}}\mathbf{u})^{\circ 2}, \quad (7)$$

where $\boldsymbol{\Delta}_{\mathrm{z}}$ and $\mathbf{A}_{\mathrm{z}} \in \mathbb{R}^{N\times N}$ are the difference and addition operators in the Z direction, respectively, and $\odot$, $\oslash$, and the superscript $\circ$ denote the Hadamard (element-wise) product, division, and power, respectively (see Appendix A) . For $\boldsymbol{\Delta}_{\mathrm{z}}$ and $\mathbf{A}_{\mathrm{z}}$ in (7), we adopt the following convolutional operators with an impulse response:

$$d_{\mathrm{z}}[\mathbf{m}] \triangleq \mathcal{Z}^{-1}\left\{\frac{(z_{\mathrm{x}} + 2 + z_{\mathrm{x}}^{-1})(z_{\mathrm{y}} + 2 + z_{\mathrm{y}}^{-1})(z_{\mathrm{z}} - z_{\mathrm{z}}^{-1})}{32}\right\},$$

which is an extension of a 2-D Sobel operator into 3-D, and

$$a_{\mathrm{z}}[\mathbf{m}] \triangleq \mathcal{Z}^{-1}\left\{\frac{(z_{\mathrm{x}} + 2 + z_{\mathrm{x}}^{-1})(z_{\mathrm{y}} + 2 + z_{\mathrm{y}}^{-1})(z_{\mathrm{z}} + z_{\mathrm{z}}^{-1})}{32}\right\},$$

which adds adjacent values in the Z-direction, where $\mathcal{Z}^{-1}\{\cdot\}$ denotes the 3-D inverse Z-transform. Note that $\boldsymbol{\Delta}_{\mathrm{z}}^{\intercal} = -\boldsymbol{\Delta}_{\mathrm{z}}$ and $\mathbf{A}_{\mathrm{z}}^{\intercal} = \mathbf{A}_{\mathrm{z}}$ hold.

B. Problem Setting of OCT Data Restoration

Assuming sparseness in the Z-direction difference $\boldsymbol{\Delta}_{\mathrm{z}}\mathbf{u}$ of the refractive index $\mathbf{u} = \mathbf{D}\mathbf{s}$, where $\boldsymbol{\Delta}_{\mathrm{z}}\mathbf{u}$ as an approximation of the reflectance $\mathbf{r} = \boldsymbol{\phi}(\mathbf{u})$[2], and the source coefficient $\mathbf{s}$ of the refractive index distribution $\mathbf{u}$, the problem setting is formulated as follows:

$$\hat{\mathbf{s}} = \arg\min_{\mathbf{s}\in\mathbb{R}^L} \frac{1}{2}\|\mathbf{P}\boldsymbol{\phi}(\mathbf{D}\mathbf{s}) - \mathbf{v}\|_2^2 + \lambda\|\mathbf{s}\|_1 + \eta\|\boldsymbol{\Delta}_{\mathrm{z}}\mathbf{D}\mathbf{s}\|_1, \quad \text{s.t.}\ \mathbf{u} = \mathbf{D}\mathbf{s} \in [a,b]^N, \quad (8)$$

where $\|\cdot\|_2$ and $\|\cdot\|_1$ are the ℓ_2-norm and the ℓ_1-norm, respectively; $a, b \in (0,\infty)$ are the lower and upper bounds of the voxels in $\mathbf{u}$; and $\lambda, \eta \in [0,\infty)$ denote the regularization parameters. The reflectance distribution $\mathbf{r}$ can be estimated as $\hat{\mathbf{r}} = \boldsymbol{\phi}(\mathbf{D}\hat{\mathbf{s}})$.

Algorithm 1 Primal-dual splitting (PDS) algorithm [18]

Input: $\mathbf{x}^{(0)}$, $\mathbf{y}^{(0)}$
Output: $\mathbf{x}^{(n)}$
1: $n \leftarrow 0$
2: **while** A stopping criterion is not satisfied **do**
3: $\quad \mathbf{x}^{(n+1)} = \mathrm{prox}_{\gamma_1 g}\left(\mathbf{x}^{(n)} - \gamma_1(\nabla f(\mathbf{x}^{(n)}) + \mathbf{L}^{\intercal}\mathbf{y}^{(n)})\right)$
4: $\quad \mathbf{y}^{(n+1)} = \mathrm{prox}_{\gamma_2 h^*}\left(\mathbf{y}^{(n)} + \gamma_2\mathbf{L}(2\mathbf{x}^{(n+1)} - \mathbf{x}^{(n)})\right)$
5: $\quad n \leftarrow n + 1$
6: **end while**

C. Linear Approximation of $\boldsymbol{\phi}(\cdot)$

Although the original $\boldsymbol{\phi}(\cdot)$ in (7) is differentiable (see Appendix A), it is nonlinear and may violate the convexity of the problem in (8). Thus, we propose a linear approximation of $\boldsymbol{\phi}(\cdot)$ for the domain that is assumed to be the refractive index. Our linear approximation of $\boldsymbol{\phi}(\cdot)$ is expressed as follows:

$$\boldsymbol{\phi}_1(\mathbf{u}) = -\beta_1(a,b)\boldsymbol{\Delta}_{\mathrm{z}}\mathbf{u}, \quad (9)$$

where $\beta_1(a,b) = 2|b-a|/(b+a)^2$, which is derived from (4) and the spectrum norm of $\{d_{\mathrm{z}}[\mathbf{m}]\}_{\mathbf{m}}$. Equation (9) guarantees that the response is null when $\mathfrak{n}_1 = \mathfrak{n}_2$ and $\mathbf{r} = \boldsymbol{\phi}_1(\mathbf{u}) \in (-1,1)^N$.

The derivative of $\boldsymbol{\phi}_1(\cdot)$ with respect to $\mathbf{u}$ is given as

$$\frac{\partial\boldsymbol{\phi}_1}{\partial\mathbf{u}} = -\beta_1(a,b)\boldsymbol{\Delta}_{\mathrm{z}} = \beta_1(a,b)\boldsymbol{\Delta}_{\mathrm{z}}^{\intercal}, \quad (10)$$

where $[\partial\mathbf{f}/\partial\mathbf{x}]_{n,m} \triangleq \partial[\mathbf{f}]_n/\partial[\mathbf{x}]_m$. In addition, $[\cdot]_n$ and $[\cdot]_{n,m}$ denote the n-th element of the vector, and the (n,m)-th element of the matrix, respectively.

D. Restoration Algorithm

The main contribution of this study is the attribution of (8) to a convex optimization problem by means of the approximation in III-C. Consequently, solvers can be obtained from both PDS and ADMM. We mainly adopt the PDS algorithm to solve the problem in (8) because inverse matrix operations are not requested. Although the proximal gradient method also does not require an inverse matrix operation, it is not adopted because the last regularization term in (8) is not proximable.

The PDS algorithm can solve problems in the following form:

$$\hat{\mathbf{x}} = \arg\min_{\mathbf{x}\in\mathbb{R}^L} f(\mathbf{x}) + g(\mathbf{x}) + h(\mathbf{L}\mathbf{x}), \quad (11)$$

where $f\colon \mathbb{R}^L \to \mathbb{R}\cup\{\infty\}$, $g\colon \mathbb{R}^L \to \mathbb{R}\cup\{\infty\}$, and $h\colon \mathbb{R}^K \to \mathbb{R}\cup\{\infty\}$ are the proper lower semi-continuous

[2]Although $\|\phi(\mathbf{u})\|_1 = \|\boldsymbol{\Delta}_{\mathbf{z}}\mathbf{u}\|_1$ is not met, $\|\phi(\mathbf{u})\|_0 = \|\boldsymbol{\Delta}_{\mathbf{z}}\mathbf{u}\|_0$ holds, where $\|\cdot\|_0$ is the pseudo ℓ_0-norm, i.e., the number of nonzero elements.

Algorithm 2 PDS for solving the problem in (8)

Input: $\mathbf{s}^{(0)}$, $\mathbf{y}_1^{(0)}$, $\mathbf{y}_2^{(0)}$
Output: $\mathbf{s}^{(n)}$
$\mathbf{u}^{(0)} = \mathbf{D}\mathbf{s}^{(0)}$, $n \leftarrow 0$
while A stopping criterion is not satisfied **do**
  $\mathbf{t} \leftarrow \mathbf{D}^\intercal(\nabla\mathcal{F}(\mathbf{u}^{(n)}) + \boldsymbol{\Delta}_{\mathrm{z}}^\intercal \mathbf{y}_1^{(n)} + \mathbf{y}_2^{(n)})$
  $\mathbf{s}^{(n+1)} = \mathfrak{G}_{\lambda\|\cdot\|_1}(\mathbf{s}^{(n)} - \gamma_1 \mathbf{t}, \gamma_1^{\frac{1}{2}})$
  $\mathbf{u}^{(n+1)} = \mathbf{D}\mathbf{s}^{(n+1)}$
  $\mathbf{q} \leftarrow 2\mathbf{u}^{(n+1)} - \mathbf{u}^{(n)}$
  $\mathbf{y}_1^{(n)} \leftarrow \mathbf{y}_1^{(n)} + \gamma_2 \boldsymbol{\Delta}_{\mathrm{z}} \mathbf{q}$
  $\mathbf{y}_2^{(n)} \leftarrow \mathbf{y}_2^{(n)} + \gamma_2 \mathbf{q}$
  $\mathbf{y}_1^{(n+1)} = \mathbf{y}_1^{(n)} - \gamma_2 \mathfrak{G}_{\eta\|\cdot\|_1}(\gamma_2^{-1}\mathbf{y}_1^{(n)}, \gamma_2^{-\frac{1}{2}})$
  $\mathbf{y}_2^{(n+1)} = \mathbf{y}_2^{(n)} - \gamma_2 P_{[a,b]^N}(\gamma_2^{-1}\mathbf{y}_2^{(n)})$
  $n \leftarrow n + 1$
end while
$\hat{\mathbf{r}} = \boldsymbol{\phi}_1(\mathbf{D}\mathbf{s}^{(n)})$

convex functions; $\nabla f(\cdot)$ is μ-Lipschitz continuous; and $\mathbf{L} \in \mathbb{R}^{K\times L}$.

Algorithm 1 shows the steps of the PDS [18], where $\mathrm{prox}_{\mathcal{G}}(\cdot)$ and $\mathrm{prox}_{\mathcal{G}^*}(\cdot)$ denote the proximal maps of the function $\mathcal{G}$ and its convex conjugate $\mathcal{G}^*$, respectively. The symbols γ_1 and γ_2 are the step size parameters set to satisfy $\gamma_1^{-1} - \gamma_2(\sigma_{\max}(\mathbf{L}))^2 \geq \mu/2$, where $\sigma_{\max}(\mathbf{L})$ is the maximum singular value of $\mathbf{L}$ [18]. To apply the PDS algorithm to the problem in (8), let

$$f(\mathbf{x}) = \mathcal{F}(\mathbf{D}\mathbf{x}) = \frac{1}{2}\left\|\mathbf{P}\boldsymbol{\phi}_1(\mathbf{D}\mathbf{x}) - \mathbf{v}\right\|_2^2, \tag{12a}$$

$$g(\mathbf{x}) = \lambda\|\mathbf{x}\|_1, \tag{12b}$$

$$h(\mathbf{L}\mathbf{x}) = \eta\|\mathbf{y}_1\|_1 + \imath_{[a,b]^N}(\mathbf{y}_2), \tag{12c}$$

$$\mathbf{L}\mathbf{x} = \begin{bmatrix}\mathbf{y}_1\\ \mathbf{y}_2\end{bmatrix} = \begin{bmatrix}\boldsymbol{\Delta}_{\mathrm{z}}\mathbf{D}\\ \mathbf{D}\end{bmatrix}\mathbf{x}, \tag{12d}$$

where $\imath_C(\mathbf{x})$ denotes the indicator function defined as 0 for $\mathbf{x} \in C$ and ∞ for $\mathbf{x} \notin C$. We then obtain the PDS steps with hierarchical sparsity with a hard constraint, as shown in Algorithm 2 (see Appendix B). If synthesis dictionary $\mathbf{D}$ satisfies the Parseval tight property, i.e., $\mathbf{D}\mathbf{D}^\intercal = \mathbf{I}$ [25], [26], then $\sigma_{\max}(\mathbf{L}) = \sigma_{\max}\left(\left[\begin{smallmatrix}\boldsymbol{\Delta}_{\mathrm{z}}\\ \mathbf{I}\end{smallmatrix}\right]\right)$ holds, where $\mathbf{I}$ denotes the identity matrix. For example, orthonormal transforms, such as the discrete cosine transform, the undecimated Haar transform (UDHT) [27], and non-separable oversampled lapped transform [28] satisfy the tight Parseval condition. Once we have the estimation of coefficients $\hat{\mathbf{s}}$, the reflectance distribution $\mathbf{r}$ is estimated as $\hat{\mathbf{r}} = \boldsymbol{\phi}_1(\mathbf{D}\hat{\mathbf{s}})$.

In Algorithm 2, $\mathfrak{G}_{c\|\cdot\|_1}(\mathbf{x}, \sigma)$ and $P_{[a,b]^N}(\mathbf{x})$ denotes the soft-thresholding and metric projection, which are defined as follows:

$$\left[\mathfrak{G}_{c\|\cdot\|_1}(\mathbf{x}, \sigma)\right]_n \triangleq \mathrm{sgn}([\mathbf{x}]_n)\max\left\{|[\mathbf{x}]_n| - c\sigma^2, 0\right\} \tag{13}$$

and

$$\left[P_{[a,b]^N}(\mathbf{x})\right]_n \triangleq \min\{\max\{[\mathbf{x}]_n, a\}, b\}. \tag{14}$$

The gradient of $\mathcal{F}(\cdot)$ is obtained using the chain rule as

$$\begin{aligned}\nabla\mathcal{F}(\mathbf{u}) &= \left(\frac{\partial\boldsymbol{\phi}_1}{\partial\mathbf{u}}\right)^\intercal \mathbf{P}^\intercal(\mathbf{P}\boldsymbol{\phi}_1(\mathbf{u}) - \mathbf{v})\\ &= \beta_1(a,b)\boldsymbol{\Delta}_{\mathrm{z}}\mathbf{P}^\intercal(\beta_1(a,b)\mathbf{P}\boldsymbol{\Delta}_{\mathrm{z}}^\intercal\mathbf{u} - \mathbf{v}).\end{aligned} \tag{15}$$

The Lipschitz constant of $\nabla f(\cdot)$ is determined by $\mu = (\beta_1(a,b)\sigma_{\max}(\mathbf{P}\boldsymbol{\Delta}_{\mathrm{z}}\mathbf{D}))^2$ from (10). Especially, $\mu = (\beta_1(a,b)\sigma_{\max}(\mathbf{P}\boldsymbol{\Delta}_{\mathrm{z}}))^2$ for a Parseval tight dictionary $\mathbf{D}$.

We can also derive a solver for (8) using ADMM. For the detail, see Appendix C.

E. Identification of the Measurement Process

In the previous discussions, we assumed that the measurement process $\mathbf{P}$ is known. However, the characteristics are highly dependent on the measurement device, and we need to identify the parameters before solving the problem in (8). The quantitative estimation of the measurement process $\mathbf{P}$ is essential to achieve high-quality restoration.

We reduce the identification problem to the search for optimal parameters in (2). The parameter set is expressed by

$$\boldsymbol{\theta} \triangleq [\alpha_{\mathrm{p}}, \sigma_{\mathrm{xy}}, \sigma_{\mathrm{z}}, \omega_{\mathrm{p}}, b_{\mathrm{p}}]^\intercal \tag{16}$$

and identified for a known simple array of $\{r[\mathbf{k}]\}_{\mathbf{k}}$, for example, a glass substrate.

Note that we also have to consider the nonlinear sampling process owing to the frequency variation of the piezoelectric elements. We need to adjust the variable sampling interval in the Z-direction. We obtained the frequency variation using a known sample with a simple structure and a continuous reflectance distribution. In the following section, we present specific experiment results.

IV. Performance Evaluation

In this section, we verify the significance of the proposed model through simulations conducted on artificial data before showing the experimental results in V. First, to confirm the effectiveness of introducing a latent refractive index distribution, we present some results for 1-D sequences in the Z-direction only. The validity of the proposed model is verified. In addition, convergence properties and computation time of the algorithm will be discussed. Next, we proceed to evaluation of the proposed method using 3-D volumetric data.

A. Model validation

Let us validate the effectiveness of the proposed model with latent refractive index distribution $\mathbf{u}$. Comparisons are made with a reference model that does not take $\mathbf{u}$ into account. The reference model adopts 1-D TV for reflectance distribution $\mathbf{r}$ in the Z-direction and the problem setting is given as follows:

$$\hat{\mathbf{r}} = \arg\min_{\mathbf{r}\in(-1,1)^N} \frac{1}{2}\|\mathbf{P}\mathbf{r} - \mathbf{v}\|_2^2 + \eta\left\|\mathfrak{D}_{\mathrm{z}}\mathbf{r}\right\|_1, \tag{17}$$

where $\mathfrak{D}_{\mathrm{z}}$ is the linear operator with the first-order difference filter, i.e., $(1 - z_{\mathrm{z}}^{-1})$ in the transfer function expression. The last term in (17) means the 1-D TV regularization in the Z-direction. (17) is motivated by the model adopted in [14].

Although the measurement process $\mathbf{P}$ is not considered in the article [14], (17) considers $\mathbf{P}$. In this validation, 1-D signals in the Z-direction are tentatively dealt with. Therefore, for this validation only, the following settings are temporarily adopted.

TABLE I

1-D SIMULATION SPECIFICATIONS, WHERE THE "PHANTOM" FUNCTION OF MATLAB R2022A IS USED FOR GENERATING THE 1-D SOURCE $\mathbf{u}$ WITH THE OPTION "MODIFIED SHEPP-LOGAN." THE LINE AT THE CENTER OF THE VERTICAL DIRECTION WAS EXTRACTED AS A Z-DIRECTION SEQUENCE AND THE INTENSITY WAS SCALED TO THE RANGE OF $a = 1.00$ AND $b = 1.50$. EVALUATION POINTS OF λ AND η ARE LOGARITHMICALLY SPACED BETWEEN THE INDICATED RANGE IN THIS TABLE AND ρ FOR ADMM WAS EXPERIMENTALLY SET.

	Ref. w/ PDS	Prop. w/ PDS	Prop. w/ ADMM
Source $\mathbf{u}$	1-D sequence in $[1.00, 1.50]^{256}$		
Target $\mathbf{r}$	$\boldsymbol{\phi}(\mathbf{u})$ in $(-1, 1)^{256}$		
σ_{w}	$\{0.01,\ 0.02,\ 0.03,\ 0.04,\ 0.05\ \}$		
η	16 points in [2.51e-02, 2.51e-01]		
λ	-	16 points in [1.58e-04, 1.58e-01]	
μ	100	1.817	-
$\sigma_{\max}(\mathbf{L})^2$	4	2	-
γ_1	$2/1.05\mu$		-
γ_2	$(1/\gamma_1 - \mu/2)/1.05\sigma_{\max}(\mathbf{L})^2$		-
ρ	-	-	0.016
# of iterations	1000		
# of trials	10		
Measurement process $\mathbf{P}$			
ω_{p}	0.3π		
σ_{z}	30		
b_{p}	0.05		
Synthesis dictionary $\mathbf{D}$			
Type	-	1-D Parseval tight UDHT	
# of tree levels	-	$\{1,\ 2,\ 3,\ 4,\ 5\}$	

- $\mathbf{P}$: Convolution with kernel $\{p_{\mathrm{z}}[m_{\mathrm{z}}]\}_{m_{\mathrm{z}}}$ in (2c)
- $\mathbf{D}$: 1-D Parseval tight UDHT
- $\boldsymbol{\Delta}_{\mathrm{z}}$: Convolution with kernel $\mathcal{Z}^{-1}\{(z_{\mathrm{z}} - z_{\mathrm{z}}^{-1})/2\}$
- $\mathbf{A}_{\mathrm{z}}$: Convolution with kernel $\mathcal{Z}^{-1}\{(z_{\mathrm{z}} + z_{\mathrm{z}}^{-1})/2\}$

Here we compare the following three methods:

- Algorithm 2 with proposed model (Prop. w/ PDS)
- Algorithm 4 with proposed model (Prop. w/ ADMM)
- Algorithm 5 with reference model (Ref. w/ PDS)

For the derivation of Algorithm 5, see Appendix D.

Tables I and II summarize the simulation specifications and the results, respectively. The 1-D source $\mathbf{u}$ is generated by the `phantom` function of MATLAB R2022a with the option "Modified Shepp-Logan," where the line at the center of the vertical direction was extracted as a Z-direction sequence and the intensity was scaled to the range of $[a, b] = [1.00, 1.50]$. In this simulation, we generated the observed signal 10 times with random noise and tried to restore the reflectance distribution $\mathbf{r}$. Sweeping λ and η, the average MSEs of the restored results were evaluated, and only the best results for each noise level and each method are shown. From Table II, we see that the proposed model generally achieves higher quality restoration than the reference model. As for the comparison between PDS and ADMM for the proposed model, the performances are competitive.

Fig. 5 illustrates example distributions of the simulation results, where σ_{w} is set to 0.05 and the tree level of the dictionary $\mathbf{D}$ is set to 3. The values of λ and η from Table II were used and the other settings are in Table I. From Fig. 5, we see that the restoration results of the proposed method shown in (f) and (h) fit the original reflectance distribution $\mathbf{r}$ better than that of the reference method shown in (d), which is also confirmed by the MSE values. In order to estimate the original

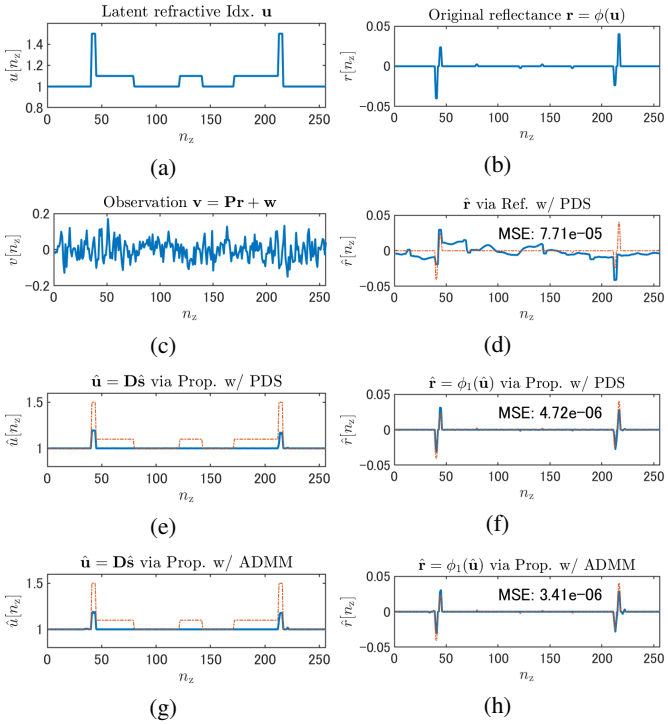

Fig. 5. Examples of 1-D simulation results by Ref. w/ PDS, Prop. w/ PDS and Prop. w/ ADMM with σ_{w} set to 0.05 and the tree level of the dictionary $\mathbf{D}$ set to 3, where the values of λ and η from Table II were used. Other settings are shown in Table I. (a) is the source refractive index distribution $\mathbf{u}$, (b) is the reflectance distribution $\mathbf{r}$, (c) is the observed signal $\mathbf{v}$, (d) is the result of restoring $\mathbf{r}$ by Ref. /w PDS, (e) and (f) are the results of restoring $\mathbf{u}$ and $\mathbf{r}$ by Prop. w/ PDS, respectively, (g) and (h) are the results of restoring $\mathbf{u}$ and $\mathbf{r}$ by Prop. w/ ADMM, respectively. The dashed lines in (d), (f), and (h) indicate the original $\mathbf{r}$, and the dashed lines in (e) and (g) indicate the original $\mathbf{u}$.

signal $\mathbf{r}$ from the observed signal $\mathbf{v}$ hidden in the noise shown in (c), we can validate the effectiveness of assuming latent refractive index distribution shown in (a) as a prior. Fig. 5 (e) and (g) show that the refractive index distribution $\mathbf{u}$ is also estimated; the tendency for $\mathbf{u}$ to be underestimated is due to the higher sensitivity of the approximation $\boldsymbol{\phi}_1(\cdot)$ than the original $\boldsymbol{\phi}(\cdot)$.

Fig. 6 compares the computational complexities among Ref. w/ PDS, Prop. w/ PDS and Prop. w/ ADMM. Fig. 6 (a) and (b) show the convergence characteristics and processing time per iteration required to obtain the simulation results shown in Fig. 5, respectively. From Fig. 6 (a), we see that the proposed methods have better restoration performance than the reference method, and in particular, the ADMM approach converges faster for iterations. However, Fig. 6 (b) shows that the reference method is lightweight, while the proposed methods require more computation in an iteration. In particular, the ADMM approach is computationally expensive. Although it highly depends on the implementation method, especially of the inverse operation by $\mathbf{Q}^{-1}$ in (38), we must be careful in its application to volumetric data. Hereafter, we will adopt Prop. w/ PDS, which offers an appropriate balance between quality and computational cost.

TABLE II

SIMULATION RESULTS OF 1-D REFLECTANCE RESTORATION IN TERMS OF AVERAGE MSE, WHERE "LV." DENOTES THE NUMBER OF TREE LEVELS OF UDHT. THE BOLDFACE HIGHLIGHTS THE BEST VALUES AT EACH NOISE LEVEL. TABLE I SUMMARISES THE SPECIFICATIONS OF THIS SIMULATION.

σ_{w}		0.01		0.02		0.03		0.04		0.05	
Method	Lv.	MSE	$\frac{\lambda}{\eta}$	MSE	$\frac{\lambda}{\eta}$	MSE	$\frac{\lambda}{\eta}$	MSE	$\frac{\lambda}{\eta}$	MSE	$\frac{\lambda}{\eta}$
Ref. w/ PDS	-	1.80e-05	$\frac{-}{6.31e-02}$	2.47e-05	$\frac{-}{1.00e-01}$	3.94e-05	$\frac{-}{1.17e-01}$	5.16e-05	$\frac{-}{1.58e-01}$	6.49e-05	$\frac{-}{1.85e-01}$
Prop. w/ PDS	1	2.28e-06	$\frac{3.98e-03}{5.41e-02}$	3.40e-06	$\frac{2.51e-03}{5.41e-02}$	4.89e-06	$\frac{3.98e-03}{5.41e-02}$	1.10e-05	$\frac{2.51e-03}{6.31e-02}$	1.70e-05	$\frac{3.98e-03}{6.31e-02}$
	2	2.31e-06	$\frac{3.98e-03}{5.41e-02}$	3.22e-06	$\frac{2.51e-03}{5.41e-02}$	4.45e-06	$\frac{3.98e-03}{5.41e-02}$	1.05e-05	$\frac{3.98e-03}{6.31e-02}$	1.48e-05	$\frac{3.98e-03}{5.41e-02}$
	3	2.41e-06	$\frac{2.51e-03}{4.64e-02}$	3.47e-06	$\frac{2.51e-03}{5.41e-02}$	5.14e-06	$\frac{2.51e-03}{4.64e-02}$	1.24e-05	$\frac{2.51e-03}{5.41e-02}$	1.66e-05	$\frac{2.51e-03}{5.41e-02}$
	4	6.62e-06	$\frac{6.31e-04}{5.41e-02}$	9.31e-06	$\frac{1.58e-03}{3.41e-02}$	9.69e-06	$\frac{1.58e-03}{3.98e-02}$	1.54e-05	$\frac{2.51e-03}{5.41e-02}$	1.77e-05	$\frac{2.51e-03}{5.41e-02}$
	5	6.18e-06	$\frac{1.58e-03}{3.98e-02}$	8.04e-06	$\frac{1.58e-03}{3.98e-02}$	9.10e-06	$\frac{1.58e-03}{3.98e-02}$	1.52e-05	$\frac{2.51e-03}{5.41e-02}$	1.57e-05	$\frac{2.51e-03}{5.41e-02}$
Prop. w/ ADMM	1	4.91e-06	$\frac{6.31e-03}{3.41e-02}$	6.18e-06	$\frac{6.31e-03}{4.64e-02}$	1.05e-05	$\frac{6.31e-03}{3.98e-02}$	1.71e-05	$\frac{2.51e-03}{7.36e-02}$	1.92e-05	$\frac{6.31e-04}{6.31e-02}$
	2	5.58e-06	$\frac{1.58e-03}{6.31e-02}$	6.61e-06	$\frac{6.31e-03}{4.64e-02}$	1.04e-05	$\frac{6.31e-03}{3.98e-02}$	1.72e-05	$\frac{2.51e-03}{7.36e-02}$	1.92e-05	$\frac{6.31e-04}{6.31e-02}$
	3	**2.17e-06**	$\frac{3.98e-03}{5.41e-02}$	**2.63e-06**	$\frac{3.98e-03}{5.41e-02}$	**4.15e-06**	$\frac{3.98e-03}{5.41e-02}$	**8.99e-06**	$\frac{3.98e-03}{6.31e-02}$	**1.40e-05**	$\frac{3.98e-03}{5.41e-02}$
	4	8.47e-06	$\frac{1.00e-03}{4.64e-02}$	9.97e-06	$\frac{1.00e-03}{5.41e-02}$	1.17e-05	$\frac{6.31e-04}{4.64e-02}$	1.76e-05	$\frac{6.31e-04}{6.31e-02}$	1.86e-05	$\frac{6.31e-04}{6.31e-02}$
	5	8.12e-06	$\frac{1.00e-03}{4.64e-02}$	9.50e-06	$\frac{1.00e-03}{5.41e-02}$	1.06e-05	$\frac{1.58e-03}{3.98e-02}$	1.59e-05	$\frac{2.51e-03}{5.41e-02}$	1.65e-05	$\frac{2.51e-03}{6.31e-02}$

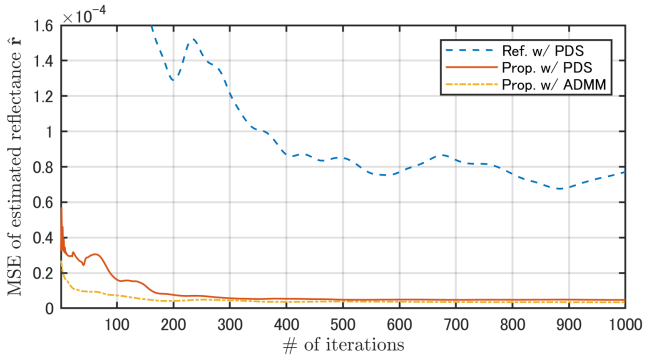

(a)

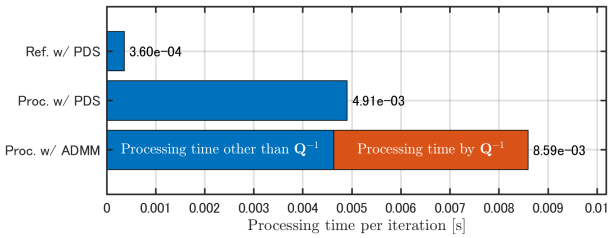

(b)

Fig. 6. Comparison of computational complexities among Ref. w/ PDS, Prop. w/ PDS and Prop. w/ ADMM. (a) and (b) show the convergence characteristics and processing time per iteration required to obtain the simulation results shown in Fig. 5, respectively, where MATLAB R2022a on a 64-bit Windows platform with an Intel Core i7 CPU is used. The process by $\mathbf{Q}^{-1}$ in Step 3 of Algorithm 4 was realized by a linear process corresponding to (38).

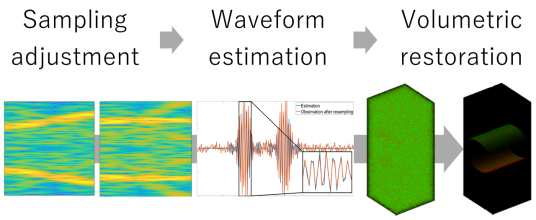

Fig. 7. Flow of the proposed restoration method. During the "sampling adjustment" stage, the peak frequency is detected, which is distorted by the piezoelectric element, applied as a constant. By adjusting the sampling interval, the peak frequency of the STFT also becomes a constant. During the "waveform estimation" stage, the interference waveform is estimated based on the assumption that the peak frequency is constant. During the "volumetric restoration" stage, contaminated 3-D volumetric data are restored based on the parameters identified through experiments conducted to obtain clear volumetric data from noisy data.

B. Restoration Simulation

The flow of the restoration process applied during the simulations and experiments is shown in Fig. 7. In the following, $\mathbf{\Delta}_{\mathrm{z}}$ and $\mathbf{A}_{\mathrm{z}}$ are reverted back to the original 3-D system in III-A. In addition, a 3-D dictionary is adopted as the synthesis dictionary $\mathbf{D}$. The simulation was conducted under the following conditions:

1) Sampling adjustment simulation for artificial opaque-tape data with scattered reflection points
2) Interference waveform estimation with an artificial thin glass substrate having two sharp reflection points in the Z-direction
3) Restoration simulation with Modified Shepp-Logan volumetric data as a refractive index distribution

A measurement process is shared by all of the following simulations, and the observation is set to a size of $64\times64\times300$ voxels.

1) Sampling adjustment: First, let us conduct simulations on a sampling adjustment. In a real OCT device, the nonlinearity of the piezoelectric actuator violates the constant interval of the sampling points in the Z-direction. Thus, we have to determine the misalignment and compensate for the inconstant interval. The short-time Fourier transform (STFT) can be used to identify the sampling interval in the Z-direction. In principle, the angular frequency ω_{p} in (2c) should be constant. Thus, we can detect the misalignment from the variation in the peak frequency of the monitored coherence function $p[\mathbf{m}]$. Based on the identified sampling interval, we can compensate the misalignment such that the peak frequency is constant. In this study, the peak frequency variation was assumed to be

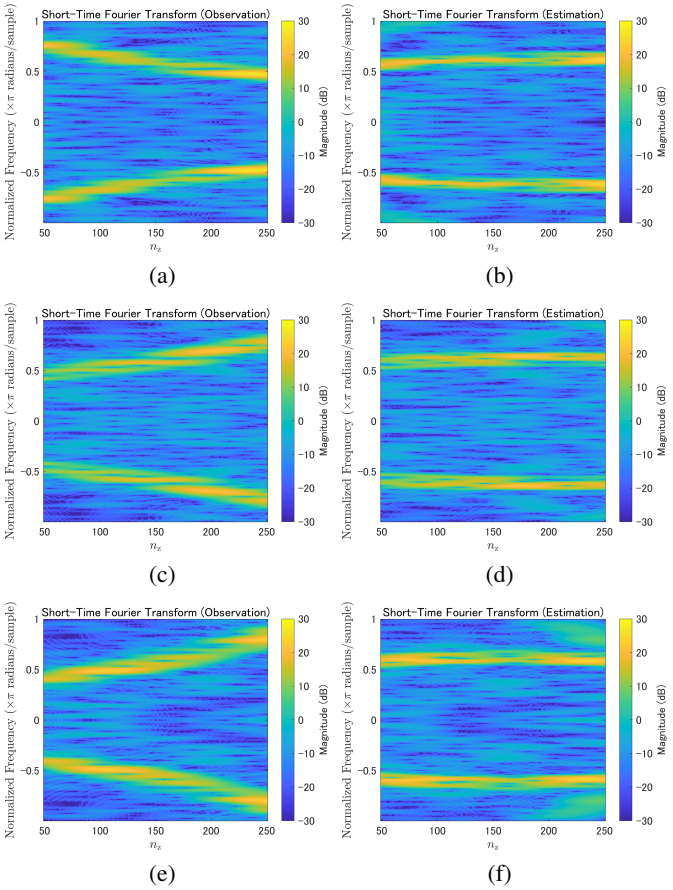

Fig. 8. Simulation results of the sampling adjustment are shown using the STFT. The STFT was performed using a hamming window with a length of 100. (a), (c), and (e) OCT observations of opaque-tape data before a sampling adjustment, where the angular frequencies ω_{p} are set from 0.8π to 0.4π, 0.4π to 0.8π, and 0.3π to 0.9π, respectively, and the noise level σ_{w} was set to 0.05. (b), (d), and (f) OCT observations after the sampling adjustment from the results of (a), (c), and (e), respectively.

linear.

In the following simulation, the reflectance distribution of the artificial opaque-tape was modeled as

$$r[\mathbf{k}] = e[\mathbf{k}] + c[\mathbf{k}], \tag{18}$$

where $e[\mathbf{k}]$ represents the edges

$$e[\mathbf{k}] = \begin{cases} 0.3 & k_{\mathrm{z}} = 75 \\ -0.3 & k_{\mathrm{z}} = 225 \\ 0 & \text{o.w.} \end{cases} \tag{19}$$

and $c[\mathbf{k}]$ denotes the scatters modeled through a Gaussian distribution with zero mean and a standard deviation of 0.1. In addition, the angular frequency ω_{p} was artificially set.

The simulation results for the artificial data are shown in Fig. 8, where the "`stft`," "`polyfit`" and "`resampling`" functions in MATLAB R2022a were used. Fig. 8 shows that the angular frequency remains almost unchanged after the sampling adjustment. In addition, the error was approximately 1.5%.

2) Interference waveform estimation: Second, we conducted a simulation on the interference waveform estimation. The unknown interference waveform parameter set $\boldsymbol{\theta}$ of (16) is

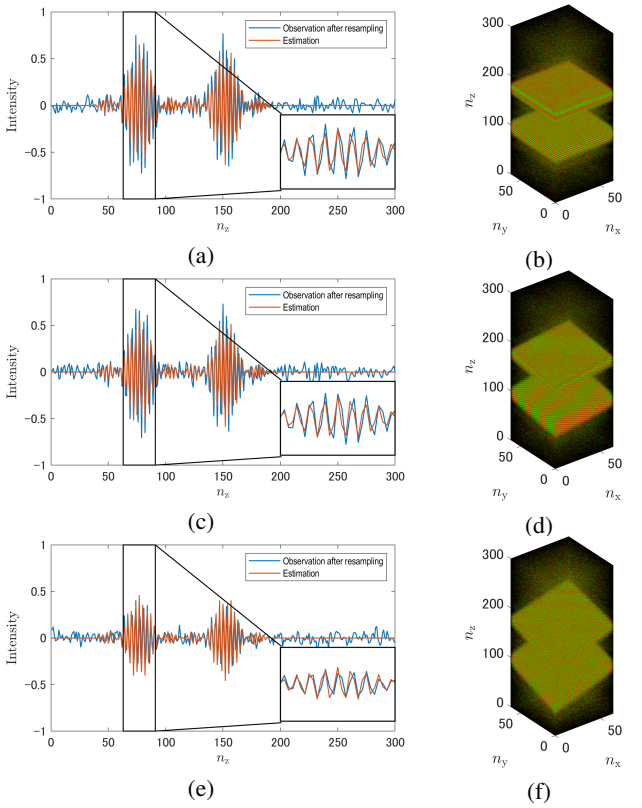

Fig. 9. Simulation results of the interference waveform estimation. (a), (c), and (e) Comparison between observations after sampling adjustment as in Fig. 8 (c)(d), estimation and fit condition of the estimated interference waveform, where the slopes $\mathbf{a}_{\mathrm{r}} = a_{\mathrm{r}}[1, 1]^{\intercal}$ of the artificial glass surfaces in (a), (c), and (e) are 0, 0.25, and 0.5, respectively. (b), (d), and (f) Observed signals before the sampling adjustment, which are the artificial data used in (a), (c), and (e), respectively.

identified using a known reflectance distribution with a simple structure. In the identification, the gradient descent method is used to search for an optimum parameter set (see Appendix E). In this simulation, we assumed a slanted artificial thin glass for the reflectance distribution and defined the model as

$$r[\mathbf{k}] = \begin{cases} 0.5 & k_{\mathrm{z}} = \mathrm{round}(75 + a_{\mathrm{rx}}k_{\mathrm{x}} + a_{\mathrm{ry}}k_{\mathrm{y}}) \\ -0.5 & k_{\mathrm{z}} = \mathrm{round}(150 + a_{\mathrm{rx}}k_{\mathrm{x}} + a_{\mathrm{ry}}k_{\mathrm{y}}) \\ 0 & \text{o.w.} \end{cases}, \tag{20}$$

where $\mathbf{a}_{\mathrm{r}} = [a_{\mathrm{rx}}, a_{\mathrm{ry}}]^{\intercal}$ is the inclination of the glass surface. The interference waveform is estimated using the response from this artificial glass data. The simulation configuration is as follows:

- The root mean of the power spectrum in the Z direction was calculated for the sampling-adjusted observation data, and its Gaussian fitting result is empirically used to set the initial values of α_{p}, ω_{p}, and σ_{z},
- the other parameters in $\boldsymbol{\theta}$ are randomly initialized through a uniform distribution with a mean value of the ground truth with a $\pm 50\%$ range,
- $\boldsymbol{\theta}$ is optimized using a gradient descent and
- the number of iterations is set to 1000.

The results of this simulation are shown in Fig. 9. From Fig. 9, we can observe that the waveforms fit well. The

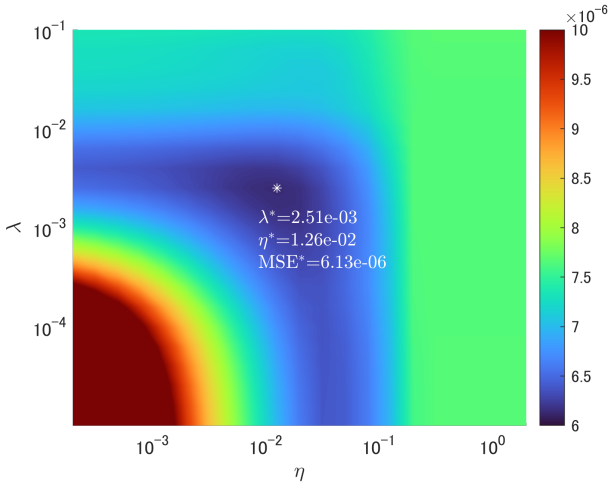

Fig. 10. MSE validation for sparse regularization parameters λ and η. This evaluation was conducted for an observation $\mathbf{v}$ of size $64 \times 64 \times 300$ through the oracle measurement process $\mathbf{P}$ with AWGN of standard deviation $\sigma_{\rm w} = 0.05$, where $\alpha_{\rm p} = 1$, $\sigma_{\rm z} = 30$, $\sigma_{\rm xy} = 0.5$, $\omega_{\rm p} = 0.6\pi$, $b_{\rm p} = 0.05$, $\gamma_1 = 2.86 \times 10^{-1}$, $\gamma_2 \simeq 7.93 \times 10^{-2}$, and the number of iterations was set to 1000. In this simulation, the two-level UDHT was used as the dictionary $\mathbf{D}$. The best combination of $\lambda^* \simeq 2.51 \times 10^{-3}$ and $\eta^* \simeq 1.26 \times 10^{-2}$ is indicated by the white asterisk in terms of the MSE.

TABLE III

SIMULATION RESULTS FOR VARIOUS NOISE LEVELS, WHERE "SAMPLING" IN (A) DENOTES THE ERROR RATE [%] BETWEEN THE TARGET INTERVAL AND ESTIMATED INTERVAL VALUE AND "WAVE" IN (A) DENOTES THE ERROR RATE [%] BETWEEN THE TARGET VALUE OF THE INTERFERENCE WAVEFORM PARAMETERS AND THAT IDENTIFIED THROUGH THE SIMULATION. THE MEAN SQUARE ERROR (MSE) IN (A) INDICATES THE RESTORATION QUALITY OF THE SIMULATION. THE VALUES WERE EVALUATED BY AVERAGING 9 TRIALS. (B) SHOWS THE ERROR RATES FOR INDIVIDUAL PARAMETERS IN THE WAVEFORM ESTIMATION.

(a)

Noise level	Sampling (%)	Wave (%)	MSE
0.1	1.46	12.1	5.73×10^{-6}
0.2	1.45	12.3	5.80×10^{-6}
0.3	1.44	12.3	6.71×10^{-6}
0.4	1.42	12.3	6.93×10^{-6}
0.5	1.47	13.1	9.26×10^{-6}

(b)

$\sigma_{\rm w}$	$\alpha_{\rm p}$ (%)	$\sigma_{\rm xy}$ (%)	$\sigma_{\rm z}$ (%)	$\omega_{\rm p}$ (%)	$b_{\rm p}$ (%)
0.01	13.47	27.82	8.18	0.61	11.47
0.02	13.05	27.92	7.15	0.75	13.50
0.03	13.57	27.88	5.84	0.75	13.15
0.04	13.16	28.66	5.18	0.77	12.30
0.05	12.38	28.36	5.00	0.72	13.03

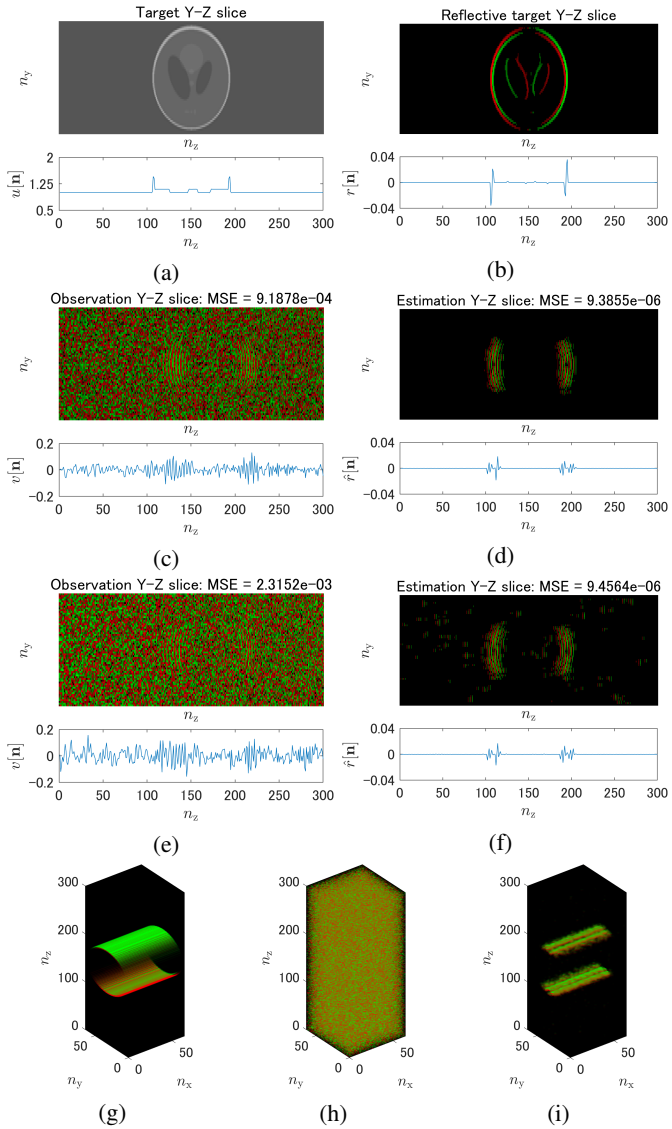

Fig. 11. Example set of artificial volumetric arrays. (Top) Y-Z slice at the center of X. (Bottom) Z-direction sequence at the center of the X-Y plane. (a) Latent refractive index distribution $\mathbf{u}$, where the `phantom` function of MATLAB R2022a is used with the option "Modified Shepp-Logan." The intensity was scaled to the range of $a = 1.00$ and $b = 1.50$. The Y-Z slice was replicated in the X-direction. (b) Reflective distribution $\mathbf{r}$ derived from $\mathbf{u}$ using the mapping $\boldsymbol{\phi}(\cdot)$ in (7). (c) Observation $\mathbf{v}$, where the AWGN of the zero mean and standard deviation of 0.03 is set as noise $\mathbf{w}$. (d) Restoration result, where MSE = 9.39×10^{-6} (e) Observation $\mathbf{v}$, where the AWGN of the standard deviation of 0.05 is set as noise $\mathbf{w}$. (f) Restoration result, where MSE = 9.46×10^{-6}. (g) The 3-D reflective distribution $\mathbf{r}$. (h) The 3-D observation $\mathbf{v}$ with the AWGN of the standard deviation 0.05 (i) The restored result $\hat{\mathbf{r}}$. The green and red voxels denote the positive and negative values, respectively. In the restoration, $\gamma_1 \simeq 2.86 \times 10^{-1}$, $\gamma_2 \simeq 7.93 \times 10^{-2}$, $\lambda = 2.51 \times 10^{-3}$, and $\eta = 1.26 \times 10^{-2}$, and the number of iterations is set to 1000, where the two-level UDHT is used as the dictionary $\mathbf{D}$.

results indicate that an unknown interference waveform can be estimated from the observations of the glass specimen. The numerical assessment is provided in Table III.

3) Volumetric data restoration: In the third stage, we conducted a restoration simulation using both the above estimated frequency fluctuation and the interference waveform. Fig. 10 shows the MSE validation of the restoration results for sparse regularization parameters λ and η with an oracle measurement process $\mathbf{P}$. The simulation results are shown in Fig. 11 and are summarized in Table III. The optimal value of λ results in 2.51×10^{-3}, where λ controls the sparsity of $\mathbf{s}$. The optimal value of η results in 1.26×10^{-2}, where η controls the total variation of $\mathbf{u}$ in the Z-direction. If λ and η deviate from the above optimal values, the restoration results worsen. It means that both terms are essential to the proposed model as the combination of the two regularization terms in (8) can provide high quality restoration. Note here that the measurement process $\mathbf{P}$ and noise level $\sigma_{\rm w}$ depend on the equipment configuration, while the synthesis model depends on the target.

It takes time to exhaustively search for parameters. However, the regularization parameters may continue to be used, as long as the characteristics of equipment and target do not change. At present, there is no good practice to set λ and η, but simulation results may be used as a reference. Figs. 11 (a) and (b) illustrate the artificial refractive index distribution $\mathbf{u}$ and reflectance distribution $\mathbf{r}$, respectively, and Figs. 11 (c) and (e) show two examples of observation $\mathbf{v}$ measured using the coherence function shown in Fig. 2 and the frequency fluctuation by the piezoelectric element, where the noise levels are set to 0.03 and 0.05, respectively. Figs. 11 (d) and (f) are the restoration results from (c) and (e), respectively. Figs. 11 (g) and (h) display the 3-D observed signal $\mathbf{v}$ and reflectance distribution $\mathbf{r}$, respectively. The simulation configuration is as follows:

- Dictionary $\mathbf{D}$ and Gaussian denoiser $\mathfrak{G}_{\mathcal{R}}(\cdot, \sigma)$:
  - 3-D 2-level UDHT [27] and soft-thresholding in (13)
- Step-size parameters:
  - $\mu \approx 6.6651$
  - $\gamma_1 = 2/(1.05\mu) \approx 2.86 \times 10^{-1}$
  - $\gamma_2 = (1.05\xi)^{-1}(1/\gamma_1 - \mu/2) \approx 7.93 \times 10^{-2}$, where $\xi = (\sigma_{\max}(\mathbf{L}))^2 = 2$
- The number of iterations is set to 1000.

Note that $\sigma_{\max}(\mathbf{L}) = \sqrt{\lambda_{\max}(\mathbf{\Delta}_{\mathrm{z}}^{\mathsf{T}}\mathbf{\Delta}_{\mathrm{z}}) + 1}$ for a tight Parseval dictionary $\mathbf{D}$, such as UDHT, where $\lambda_{\max}(\cdot)$ denotes the maximum eigenvalue.

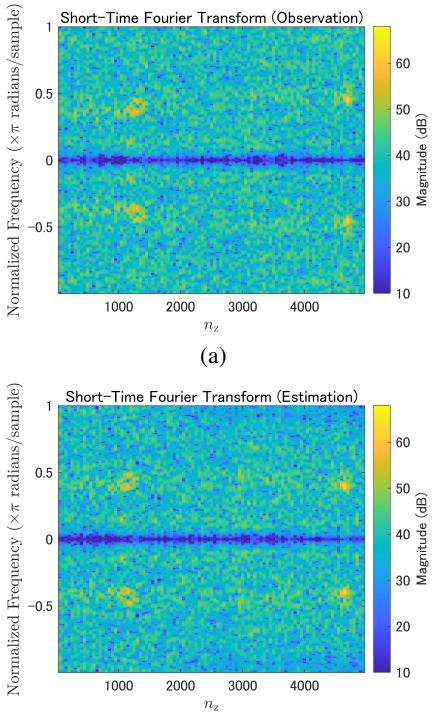

Fig. 12. Sampling adjustment result, where STFT is applied using a 100-length humming window: (a) STFT of opaque-tape data before a sampling adjustment, and (b) STFT after a sampling adjustment.

V. Experimental results

We present experimental results for an observation array of the sensory epithelium of the inner ear of a mouse measured using an MS *en-face* OCT device, which we developed. The process flow shown in Fig. 7 is adopted for the this experiment. The regularization parameters were set to $\lambda = c \times 2.51 \times 10^{-3}$ and $\eta = c \times 1.26 \times 10^{-2}$, respectively, which were the values used in IV with rescaling by a factor c of 6×10^4 set experimentally. Although it is difficult to evaluate the degree of sparsity of the refractive index distribution, we assume that some spatial correlation exists in the distribution and a sparse representation is expected through dictionary $\mathbf{D}$.

We attempt to restore an actual volumetric data observed by an MS *en-face* OCT device. The sampling adjustment result using STFT is shown in Fig. 12. Figs. 12 (a) and (b) show the STFTs before and after a sampling adjustment, respectively. It can be observed that, by adjusting the sampling interval, the peak frequency is kept constant, as in the simulation.

The results of an interference waveform estimation is shown in Fig. 13. Figs. 13 (a), (b), and (c) show the observed signal of the glass, estimated reflectance distribution of the glass, and a comparison between the observed signal and the estimated interference waveform, respectively. As in the simulation for artificial data, the observed signal and interference waveform appear similar to each other, except for the width, indicating that the interference waveform, especially the amplitude and frequency, may be successfully identified.

The results of the volumetric data restoration are shown in Figs. 14 and 15, respectively. For the observed data, the sampling adjustment parameter was calculated by itself because the measurement points of the opaque tape were different and the misalignment affects to the adjustment. According to [14], we applied the preprocessing based on median filters. Fig. 14 shows an observation of the sensory epithelium of the inner ear of a mouse[3]. Fig. 15 exhibits the restoration result of the reflectance distribution for subjective evaluation, where the problem setting similar to the simulation in Section IV-B is adopted. The data size is $64 \times 64 \times 5000$ voxels, which corresponds to a physical dimension of $0.56 \times 0.56 \times 0.37$ mm^3. The parameters of the measurement process $\mathbf{P}$ were taken from the estimation results in Fig. 13 as $\hat{\alpha}_{\mathrm{p}} = 878.4$, $\hat{\sigma}_{\mathrm{xy}} = 0.269$,

[3]The animal experiment was carried out in compliance with the protocol approved by the Institutional Animal Care and Use Committee and the President of Niigata University (Permission Number: Niigata Univ. Res. SA00458). The experiment was designed in accordance with the Japanese Animal Protection and Management Law. One male CBA/NSlc mouse (23.9 g, 7 weeks of age; SLC Inc., Hamamatsu Japan) were housed at the animal facility of Niigata University and kept on a 12 h light/12 h dark cycle. Water and food were available to the animal ad libitum. Animal handling and reporting complied with the ARRIVE guidelines [29] A combination anesthetic was prepared with 0.3 mg/kg of medetomidine (Dorbene® Vet, Kyoritsu Seiyaku Corporation, Japan), 4.0 mg/kg of midazolam (midazolam injection, Sandoz, Yamagata, Japan), and 5.0 mg/kg of butorphanol (Vetorphale, Meiji Seika Pharma Co., Ltd., Tokyo, Japan). The mouse was anesthetized adequately with an intraperitoneal injection of the anesthetic. The toe pinch, corneal reflexes, and respiratory rate were examined to evaluate the depth of anesthesia. When anesthesia was insufficient, the anesthetic was additionally injected into the animal. A tracheotomy was conducted for the maintenance of spontaneous breathing [30]. A fenestra was surgically opened on the ventrolateral site of the bulla in order to shine the low coherence light on the epithelium in the basal turn of the cochlea through the intact transparent round window. The imaging procedure of the sensory epithelium using MS *en-face* OCT was described elsewhere [9]. 5,000 *en-face* images were acquired by scanning within approximately 370μm in the axial direction. Acquisition time was 0.25 s.

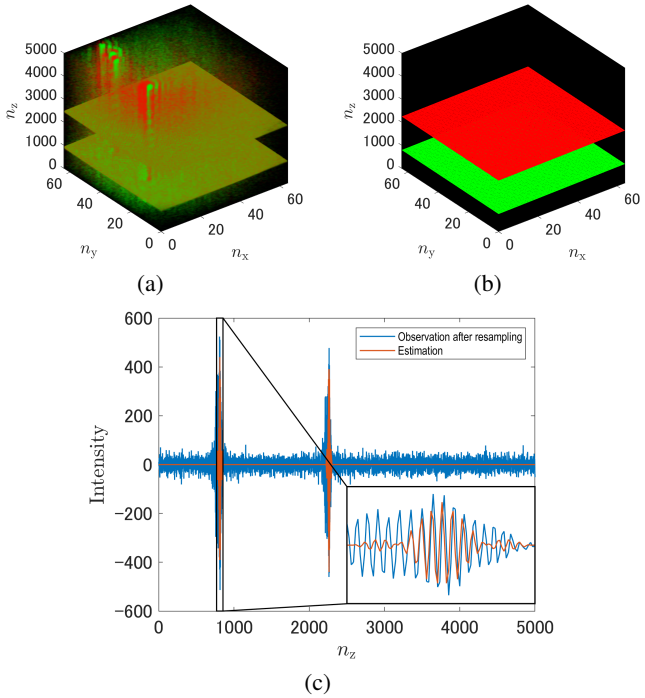

Fig. 13. Waveform estimation results for real data: (a) Observation of thin glass substrate, where the strong response along the Z direction is removed by a high-pass filter as a bias and trend component as described in II-A, (b) Estimation of the thin glass substrate by plane fitting, and (c) Comparison between observation after sampling adjustment and estimation.

$\hat{\sigma}_{\mathrm{z}} = 31.87$, $\hat{\omega}_{\mathrm{p}} = 1.351$, $\hat{b}_{\mathrm{p}} = 0.049$. In the article [8], a bandpass filter was manually set up in the frequency domain for noise removal and interference waveform extraction. Fig. 16 compares the reflectance distributions obtained through the previous manual approach adopted in [8] and through the proposed computational method. It can be observed that the restoration results of the proposed method are clearer than those of the previous approach. In addition, we observed the sensory epithelial body, which was sandwiched between the bones inside the cochlea.

Note that our proposed computational method changed the bandpass filter setting in [8] to a setting of two parameters; λ and η, which enabled us to handle high-volume OCT data systematically with a high quality restoration.

VI. Conclusions

This paper proposed a restoration method for OCT volumetric data. We reduced the restoration problem to a sparsity-aware least squares minimization problem with a hard constraint and constructed an algorithm based on the PDS framework to solve the problem. The significance was verified through simulations of the artificial data and an experiment conducted on the actual MS *en-face* OCT measurement data. Although the main motivation of this study is to overcome the disadvantage of the MS *en-face* OCT device, the proposed model is also applicable to other types of OCT devices. The restoration based on the proposed model is expected to reduce the laser power while maintaining the acquisition performance.

Finally, we summarize some open problems in the proposed method.

a) Computational cost: As indicated in IV-A, the computational cost is high due to the additional regularization term. Reducing the computational cost is an issue. For the PDS approach, an acceleration method would be effective. Since the convergence characteristic of ADMM is attractive, it is expected to improve the efficiency of processing by the inverse matrix $\mathbf{Q}^{-1}$, which requires considerable computational cost.

b) Observation process: The observation process in (5) includes the measurement process $\mathbf{P}$ and AWGN $\mathbf{w}$. Whether the assumed observation model is equal to the actual observation is an important topic. In this study, we attempted to identify the measurement process $\mathbf{P}$ from actual data taken of a glass substrate. However, we have confirmed that the initial values and parameter settings for optimization have a significant impact. There is room for improvement in the identification process and evaluation of its validity.

c) Synthesis process: A fixed synthesis dictionary $\mathbf{D}$ was used in this study, although there is still room for consideration in selecting a better dictionary to represent the refractive index distribution more sparsely. Although training data for the target refractive index distribution is required, it is a possible strategy to provide dictionary $\mathbf{D}$ through training. In this case, knowing the actual distribution is another important issue.

d) Mapping $\boldsymbol{\phi}(\cdot)$: In the proposal, the mapping $\boldsymbol{\phi}(\cdot)$ from the refractive index distribution to the reflectance distribution is approximated linearly in order to sufficiently guarantee that the optimization problem is convex. However, we are unable to deny the possibility that there exists a better nonlinear approximation method that guarantees a convex optimization framework.

e) Regularization: Strategies for setting the regularization parameters λ and η should be considered in practical applications. Furthermore, the selection of the regularization is another important topic. Steps 4 and 9 of Algorithm 2 used the regularized Gaussian denoiser representation as $\mathfrak{G}_{\mathcal{R}}(\cdot)$. For those denoising methods, we set up a typical ℓ_1-norm regularization and adopted a soft thresholding process derived from the theory. However, plugging in other denoisers is also an option to be considered.

f) Speckle noise removal: For addressing speckle noise, this study adopted the assumptions of [14] and focused on the AWGN removal problem. We consider that speckle noise removal should also be incorporated into optimization for more sophisticated processing.

g) Sampling adjustment: Regarding the frequency variation of the interference waveform, this paper assumed its linearity. However, the variation is inherently nonlinear due to the characteristics of the piezoelectric element. The slope changes with depth, and there are also points that show both increases and decreases. This positional dependence also needs to be considered in both of the measurement and processing phase.

This study provides a framework for various customization, including the observation process $\mathbf{P}$ of OCT devices. Our achievement could be an important contribution to OCT imaging

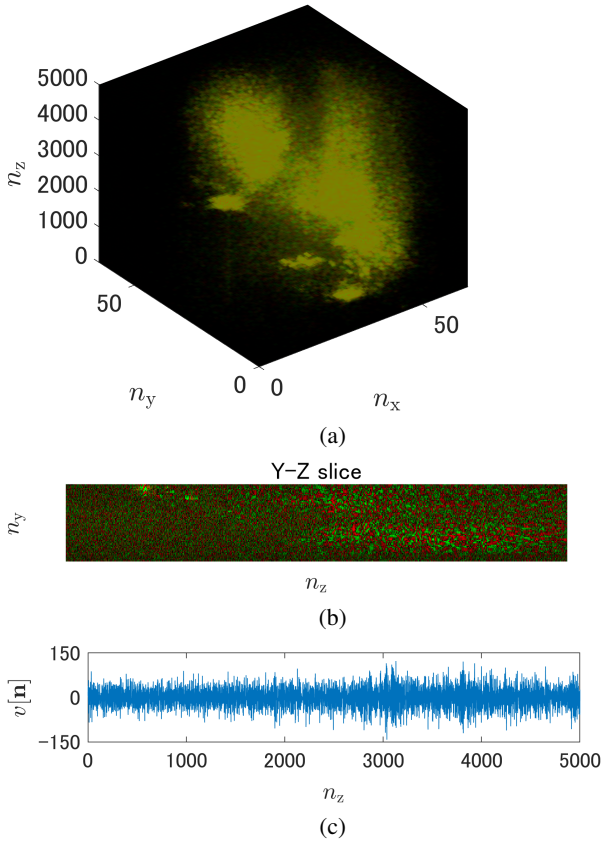

Fig. 14. The observation $\mathbf{v}$ of the sensory epithelium of an inner ear of a mouse as measured using the MS *en-face* OCT device, where bias removal was applied but not sampling adjustment: (a) 3-D representation of a $64 \times 64 \times 5000$ sized voxel corresponding to the physical dimensions of $0.56 \times 0.56 \times 0.37\text{mm}^3$, (b) Y-Z slice at the center of X, and (c) Z-direction sequence at the center of X-Y.

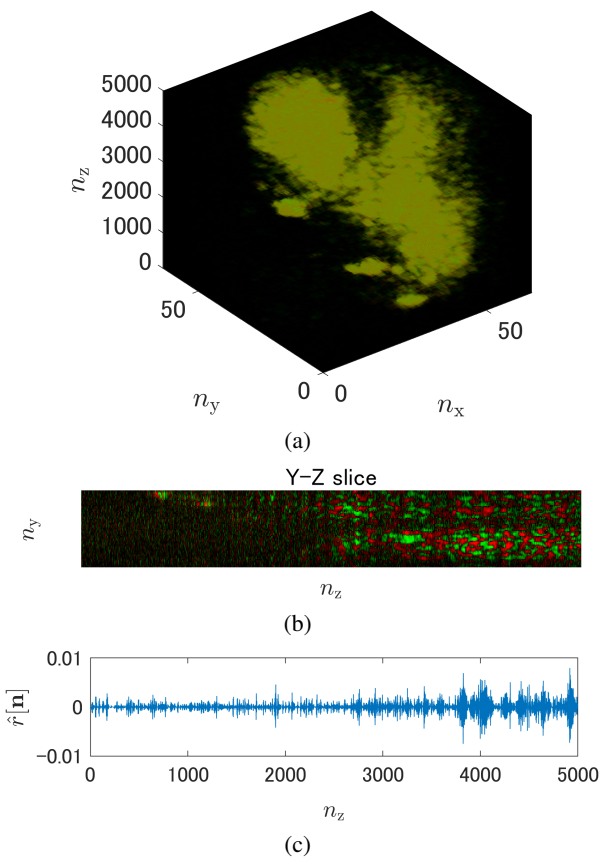

Fig. 15. Restored reflectance distribution result $\hat{\mathbf{r}} = \boldsymbol{\phi}_1(\mathbf{D}\hat{\mathbf{s}})$ using Proposed method with the PDS and two-level UDHT as $\mathbf{D}$, where preprocessing based on median filtering was applied according to [14]: (a) a 3-D representation, where the number of iterations is set to 1000, (b) a Y-Z slice at the center of X, and (c) Z-direction sequence at the center of X-Y.

Appendix A
Map $\boldsymbol{\phi}(\cdot)$ and Its Jacobian

In (4), the pairwise operations of $(\mathfrak{n}_1 + \mathfrak{n}_2)$, $(\mathfrak{n}_1 - \mathfrak{n}_2)$, and $|\mathfrak{n}_1 - \mathfrak{n}_2|$ are described as $\mathbf{A}_{\text{z}}\mathbf{u}$, $-\boldsymbol{\Delta}_{\text{z}}\mathbf{u}$, and $\text{abs}(\boldsymbol{\Delta}_{\text{z}}\mathbf{u})$, respectively, for the vector representation $\mathbf{u} \in (0,\infty)^N$ of the target volumetric data. Using the above notations, (4) can be equivalently expressed as in (7).

This appendix shows the Jacobian matrix of $\boldsymbol{\phi}(\cdot)$ in (7) to demonstrate its differentiability. Let us define $\chi(x) \triangleq |x|x$ and $\zeta(x) = x^2$ for $x \in \mathbb{R}$, and $d_n(\mathbf{u}) = [\boldsymbol{\Delta}_{\text{z}}\mathbf{u}]_n$ and $a_n(\mathbf{u}) = [\mathbf{A}_{\text{z}}\mathbf{u}]_n$ for $\mathbf{u} \in (0,\infty)^N \subset \mathbb{R}^N$. The n-th row of the Jacobian matrix of $\boldsymbol{\phi}(\cdot)$ is then expressed as

$$\begin{aligned}
\left[\frac{\partial \boldsymbol{\phi}}{\partial \mathbf{u}}\right]_{n,:} &= \frac{\partial [\boldsymbol{\phi}(\mathbf{u})]_n}{\partial \mathbf{u}} = -\frac{\partial}{\partial \mathbf{u}} \frac{\chi(d_n(\mathbf{u}))}{\zeta(a_n(\mathbf{u}))}. \\
&= -\frac{\frac{\partial \chi(d_n(\mathbf{u}))}{\partial \mathbf{u}} \zeta(a_n(\mathbf{u})) - \chi(d_n(\mathbf{u})) \frac{\partial \zeta(a_n(\mathbf{u}))}{\partial \mathbf{u}}}{\zeta(a_n(\mathbf{u}))^2}. \\
&= -2\frac{|[\boldsymbol{\Delta}_{\text{z}}\mathbf{u}]_n|\,[\mathbf{A}_{\text{z}}\mathbf{u}]_n[\boldsymbol{\Delta}_{\text{z}}]_{n,:} - |[\boldsymbol{\Delta}_{\text{z}}\mathbf{u}]_n|\,[\boldsymbol{\Delta}_{\text{z}}\mathbf{u}]_n[\mathbf{A}_{\text{z}}]_{n,:}}{[\mathbf{A}_{\text{z}}\mathbf{u}]_n^3} \\
&= -2\frac{|[\boldsymbol{\Delta}_{\text{z}}\mathbf{u}]_n|}{[\mathbf{A}_{\text{z}}\mathbf{u}]_n^3} \left([\mathbf{A}_{\text{z}}\mathbf{u}]_n[\boldsymbol{\Delta}_{\text{z}}]_{n,:} - [\boldsymbol{\Delta}_{\text{z}}\mathbf{u}]_n[\mathbf{A}_{\text{z}}]_{n,:}\right), \quad (21)
\end{aligned}$$

where $[\cdot]_{n,:}$ indicates the n-th row vector of the argument, and we apply the chain rule to derive the following relations:

$$\begin{aligned}
\frac{\partial \chi(d_n(\mathbf{u}))}{\partial \mathbf{u}} &= \frac{\partial \chi(d_n)}{\partial d_n}\frac{\partial d_n}{\partial \mathbf{u}} = 2|d_n|\frac{\partial d_n}{\partial \mathbf{u}} \\
&= 2\,|[\boldsymbol{\Delta}_{\text{z}}\mathbf{u}]_n|\,[\boldsymbol{\Delta}_{\text{z}}]_{n,:}\,, \quad (22)
\end{aligned}$$

$$\begin{aligned}
\frac{\partial \zeta(a_n(\mathbf{u}))}{\partial \mathbf{u}} &= \frac{\partial \zeta(a_n)}{\partial a_n}\frac{\partial a_n}{\partial \mathbf{u}} = 2a_n\frac{\partial a_n}{\partial \mathbf{u}} \\
&= 2[\mathbf{A}_{\text{z}}\mathbf{u}]_n[\mathbf{A}_{\text{z}}]_{n,:}\,. \quad (23)
\end{aligned}$$

Finally, we have the Jacobian matrix

$$\begin{aligned}
&\frac{\partial \boldsymbol{\phi}}{\partial \mathbf{u}} = \\
&-2\frac{\text{diag}(\text{abs}(\boldsymbol{\Delta}_{\text{z}}\mathbf{u}))}{\text{diag}(\mathbf{A}_{\text{z}}\mathbf{u})^3}\left(\text{diag}(\mathbf{A}_{\text{z}}\mathbf{u})\boldsymbol{\Delta}_{\text{z}} - \text{diag}(\boldsymbol{\Delta}_{\text{z}}\mathbf{u})\mathbf{A}_{\text{z}}\right). \quad (24)
\end{aligned}$$

Appendix B
Derivation of Algorithm 2

This appendix shows the derivation process of Algorithm 2 through the PDS framework.

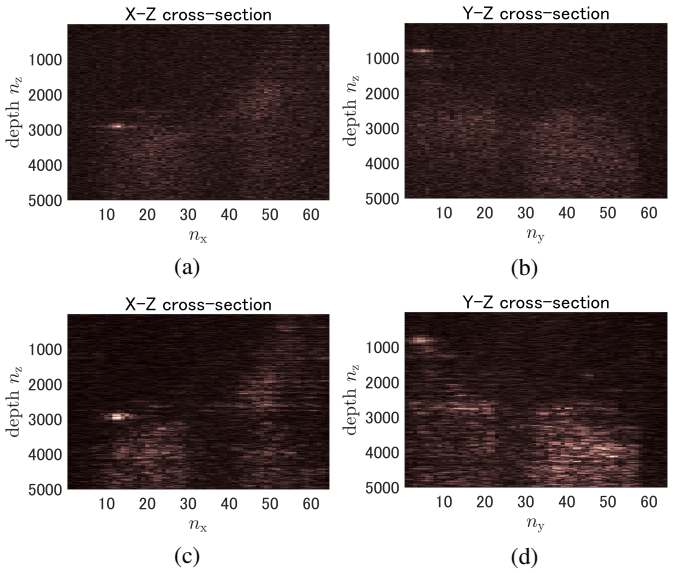

Fig. 16. Comparison between the previous manual approach and proposed computational approach. The restoration results are displayed as absolute values of the reflectance distribution $\mathrm{abs}(\hat{\mathbf{r}})$: (a) X-Z cross-section at $n_{\mathrm{x}} = 30$ and (b) Y-Z cross-section at $n_{\mathrm{y}} = 30$ using the previous method, and (c) X-Z cross-section at $n_{\mathrm{y}} = 30$ and (d) Y-Z cross-section at $n_{\mathrm{x}} = 30$ using the proposed method.

1) Step 3 in Algorithm 1: From (12a) and (12d), we have

$$\nabla f(\mathbf{x}) = \mathbf{D}^{\intercal} \nabla \mathcal{F}(\mathbf{D}\mathbf{x}) \tag{25}$$

$$\mathbf{L}^{\intercal}\mathbf{y} = \mathbf{D}^{\intercal}(\boldsymbol{\Delta}_{\mathrm{z}}^{\intercal}\mathbf{y}_1 + \mathbf{y}_2) \tag{26}$$

Because we can view a proximal mapping as a regularized Gaussian denoiser, we use the following notation:

$$\mathfrak{G}_g(\mathbf{x}, \sqrt{\gamma}) \triangleq \mathrm{prox}_{\gamma g}(\mathbf{x}) = \arg\min_{\mathbf{u}} \frac{1}{2\gamma}\|\mathbf{u} - \mathbf{x}\|_2^2 + g(\mathbf{u}). \tag{27}$$

We then have Steps 4–6 in Algorithm 2 from Step 2 in Algorithm 1 and (12b).

2) Step 4 in Algorithm 1: From (12c) and (12d), Step 4 in Algorithm 1 can be split into the following two steps:

$$\mathbf{y}_1^{(n+1)} = \mathrm{prox}_{\gamma_2 h_1^*}\left(\mathbf{y}_1^{(n)} + \gamma_2 \boldsymbol{\Delta}_{\mathrm{z}}\mathbf{D}(2\mathbf{x}^{(n+1)} - \mathbf{x}^{(n)})\right), \tag{28}$$

$$\mathbf{y}_2^{(n+1)} = \mathrm{prox}_{\gamma_2 h_2^*}\left(\mathbf{y}_2^{(n)} + \gamma_2 \mathbf{D}(2\mathbf{x}^{(n+1)} - \mathbf{x}^{(n)})\right). \tag{29}$$

Let $\mathbf{u} = \mathbf{D}(2\mathbf{x}^{(n+1)} - \mathbf{x}^{(n)})$. Then, Moreaus' identity

$$\mathrm{prox}_{\gamma h^*}(\mathbf{y}) = \mathbf{y} - \gamma \mathrm{prox}_{\gamma^{-1}h}(\gamma^{-1}\mathbf{y}) \tag{30}$$

allows us to express the above steps as

$$\mathbf{y}_1^{(n+1)} = \mathbf{y}_1^{(n)} + \gamma_2 \boldsymbol{\Delta}_{\mathrm{z}}\mathbf{u} - \gamma_2 \mathrm{prox}_{\gamma_2^{-1}h_1}\left(\gamma_2^{-1}\mathbf{y}_1^{(n)} + \boldsymbol{\Delta}_{\mathrm{z}}\mathbf{u}\right), \tag{31}$$

$$\mathbf{y}_2^{(n+1)} = \mathbf{y}_2^{(n)} + \gamma_2 \mathbf{u} - \gamma_2 \mathrm{prox}_{\gamma_2^{-1}h_2}\left(\gamma_2^{-1}\mathbf{y}_2^{(n)} + \mathbf{u}\right). \tag{32}$$

As a result, Steps 5–10 in Algorithm 2 are derived from Step 4 in Algorithm 1 and (12c) with $h_1(\cdot) = \eta\|\cdot\|_1$ and $h_2(\cdot) = \imath_{[a,b]^N}(\cdot)$.

Algorithm 3 Alternating direction method of multipliers (ADMM) [20], [21]

Input: $\mathbf{z}^{(0)}$, $\mathbf{d}^{(0)}$
Output: $\mathbf{x}^{(n)}$
1: $n \leftarrow 0$
2: **while** A stopping criterion is not satisfied **do**
3: $\quad \mathbf{x}^{(n+1)} = \arg\min_{\mathbf{x}} f(\mathbf{x}) + \frac{\rho}{2}\|\mathbf{z}^{(n)} - \mathbf{G}\mathbf{x} - \mathbf{d}^{(n)}\|_2^2$
4: $\quad \mathbf{z}^{(n+1)} = \mathrm{prox}_{\frac{1}{\rho}g}\left(\mathbf{G}\mathbf{x}^{(n+1)} + \mathbf{d}^{(n)}\right)$
5: $\quad \mathbf{d}^{(n+1)} = \mathbf{d}^{(n)} + \mathbf{G}\mathbf{x}^{(n+1)} - \mathbf{z}^{(n+1)}$
6: $\quad n \leftarrow n + 1$
7: **end while**

Algorithm 4 ADMM for solving the problem in (8)

Input: $\mathbf{z}^{(0)}$, $\mathbf{d}^{(0)}$
Output: $\mathbf{s}^{(n)}$
1: $\mathbf{y} = (\mathbf{P}\boldsymbol{\Phi}_1\mathbf{D})^{\intercal}\mathbf{v}$, $n \leftarrow 0$
2: **while** A stopping criterion is not satisfied **do**
3: $\quad \mathbf{s}^{(n+1)} = \mathbf{Q}^{-1}\left(\mathbf{y} + \rho\mathbf{G}^{\intercal}(\mathbf{z}^{(n)} - \mathbf{d}^{(n)})\right)$
4: $\quad \mathbf{z}_1^{(n+1)} = \mathfrak{G}_{\rho^{-1}\|\cdot\|_1}\left(\mathbf{G}_1\mathbf{s}^{(n+1)} + \mathbf{d}_1^{(n)}, \lambda^{\frac{1}{2}}\right)$
5: $\quad \mathbf{z}_2^{(n+1)} = \mathcal{P}_{[a,b]^N}\left(\mathbf{G}_2\mathbf{s}^{(n+1)} + \mathbf{d}_2^{(n)}\right)$
6: $\quad \mathbf{d}^{(n+1)} = \mathbf{d}^{(n)} + \mathbf{G}\mathbf{s}^{(n+1)} - \mathbf{z}^{(n+1)}$
7: $\quad n \leftarrow n + 1$
8: **end while**
9: $\hat{\mathbf{r}} = \boldsymbol{\phi}_1(\mathbf{D}\mathbf{s}^{(n)})$

Appendix C
Derivation of ADMM-based Algorithm

This appendix shows the derivation process of the ADMM approach [20], [21]. ADMM can solve problems in the following form:

$$\{\hat{\mathbf{x}}, \hat{\mathbf{z}}\} = \arg\min_{(\mathbf{x},\mathbf{z})\in\mathbb{R}^{L\times K}} f(\mathbf{x}) + g(\mathbf{z}) \text{ s.t. } \mathbf{z} = \mathbf{G}\mathbf{x}, \tag{33}$$

where $f\colon \mathbb{R}^L \to \mathbb{R}\cup\{\infty\}$, and $g\colon \mathbb{R}^K \to \mathbb{R}\cup\{\infty\}$ are convex functions; and $\mathbf{G} \in \mathbb{R}^{K\times L}$.

Algorithm 3 shows the steps of ADMM [20], [21]. The parameter $\rho > 0$ determines the step size. To apply the ADMM to the problem in (8), let

$$f(\mathbf{x}) = \frac{1}{2}\left\|\mathbf{P}\boldsymbol{\phi}_1(\mathbf{D}\mathbf{x}) - \mathbf{v}\right\|_2^2, \tag{34a}$$

$$g(\mathbf{z}) = \lambda\|\mathbf{z}_1\|_1 + \imath_{[a,b]^N}(\mathbf{z}_2), \tag{34b}$$

$$\mathbf{z} = \begin{bmatrix}\mathbf{z}_1\\ \mathbf{z}_2\end{bmatrix} = \begin{bmatrix}\mathbf{G}_1\\ \mathbf{G}_2\end{bmatrix}\mathbf{x} = \mathbf{G}\mathbf{x}, \tag{34c}$$

where, for $\lambda > 0$,

$$\mathbf{G}_1 = \begin{bmatrix}\mathbf{I}\\ \eta\lambda^{-1}\boldsymbol{\Delta}_{\mathrm{z}}\mathbf{D}\end{bmatrix}, \ \mathbf{G}_2 = \mathbf{D}.$$

We then obtain the ADMM steps as shown in Algorithm 4, where

$$\mathbf{Q} = (\mathbf{P}\boldsymbol{\Phi}_1\mathbf{D})^{\intercal}\mathbf{P}\boldsymbol{\Phi}_1\mathbf{D} + \rho\mathbf{G}^{\intercal}\mathbf{G}, \tag{35}$$

$$\boldsymbol{\Phi}_1 = -\beta_1(a,b)\boldsymbol{\Delta}_{\mathrm{z}}. \tag{36}$$

Since $\mathbf{G}^{\intercal}\mathbf{G} = \mathbf{I} + (\eta\lambda^{-1})^2(\boldsymbol{\Delta}_{\mathrm{z}}\mathbf{D})^{\intercal}\boldsymbol{\Delta}_{\mathrm{z}}\mathbf{D} + \mathbf{D}^{\intercal}\mathbf{D}$ is symmetric and consists of the identity matrix, it is guaranteed to be nonsingular, so is $\mathbf{Q}$.

Algorithm 5 PDS for solving the problem in (17)

Input: $\mathbf{r}^{(0)}$, $\mathbf{y}^{(0)}$
Output: $\mathbf{r}^{(n)}$
$n \leftarrow 0$
while A stopping criterion is not satisfied **do**
  $\mathbf{t} \leftarrow \mathbf{P}^\mathsf{T}(\mathbf{P}\mathbf{r}^{(n)} - \mathbf{v}) + \mathfrak{D}_\mathrm{z}^\mathsf{T}\mathbf{y}^{(n)}$
  $\mathbf{r}^{(n+1)} = \mathcal{P}_{(-1,1)^N}(\mathbf{r}^{(n)} - \gamma_1\mathbf{t})$
  $\mathbf{q} \leftarrow 2\mathbf{r}^{(n+1)} - \mathbf{r}^{(n)}$
  $\mathbf{y}^{(n)} \leftarrow \mathbf{y}^{(n)} + \gamma_2\mathfrak{D}_\mathrm{z}\mathbf{q}$
  $\mathbf{y}^{(n+1)} = \mathbf{y}^{(n)} - \gamma_2\mathfrak{G}_{\eta\|\cdot\|_1}(\gamma_2^{-1}\mathbf{y}_1^{(n)}, \gamma_2^{-\frac{1}{2}})$
  $n \leftarrow n + 1$
end while
$\hat{\mathbf{r}} = \mathbf{r}^{(n)}$

By performing the convolution operation in a circular manner, the DFT coefficient product can be used instead. Then, we have

$$\mathbf{Q} = \rho\mathbf{I} + \mathbf{D}^\mathsf{T}(\rho\mathbf{I} + \mathbf{W}^{-1}\mathbf{S}^\mathsf{T}\mathrm{diag}(\check{\mathbf{h}})\mathbf{S}\mathbf{W})\mathbf{D}, \tag{37}$$

where $\mathbf{W}$ is the DFT matrix, $\check{\mathbf{h}}$ is the vector with the non-zero entries of the frequency response of the circular convolution operator $\mathbf{\Delta}_\mathrm{z}^\mathsf{T}(\beta_1(a,b)^2\mathbf{P}^\mathsf{T}\mathbf{P} + \rho(\eta\lambda^{-1})^2\mathbf{I})\mathbf{\Delta}_\mathrm{z}$, and $\mathbf{S}$ is the subsampling matrix to extract the non-zero coefficients.

For a Parseval tight synthesis dictionary $\mathbf{D}$, $\mathbf{D}\mathbf{D}^\mathsf{T} = \mathbf{I}$ holds, and the Woodbury matrix identity gives us

$$\mathbf{Q}^{-1} = \frac{1}{\rho}\mathbf{I} - \mathbf{D}^\mathsf{T}\left(\frac{1}{2\rho}\mathbf{I} + \frac{1}{4\rho^2}\mathbf{W}^{-1}\mathbf{S}^\mathsf{T}\left(\frac{1}{2\rho}\mathbf{I} + \mathrm{diag}(\check{\mathbf{h}})^{-1}\right)^{-1}\mathbf{S}\mathbf{W}\right)\mathbf{D}. \tag{38}$$

For low-dimensional problems, $\mathbf{Q}^{-1}$ can be pre-computed. However, it is not suitable for volumetric data with high dimensionality. Instead of precomputing $\mathbf{Q}^{-1}$, we can realize the linear process by (38) by combining the synthesis operator $\mathbf{D}$, analysis operator $\mathbf{D}^\mathsf{T}$, DFT $\mathbf{W}$, its inverse $\mathbf{W}^{-1}$, subsampling $\mathbf{S}$ and zero-value insertion $\mathbf{S}^\mathsf{T}$. However, even the latter approach requires a huge amount of memory and computation for volumetric data.

Appendix D
Reference method

Algorithm 5 shows the PDS steps for the reference method motivated by [14]. The following summarizes the derivation process.

(17) is equivalently represented by

$$\hat{\mathbf{r}} = \arg\min_{\mathbf{r}\in\mathbb{R}^N} \frac{1}{2}\|\mathbf{P}\mathbf{r} - \mathbf{v}\|_2^2 + \iota_{(-1,1)^N}(\mathbf{r}) + \eta\,\|\mathfrak{D}_\mathrm{z}\mathbf{r}\|_1. \tag{39}$$

To apply PDS to the problem in (39), let

$$f(\mathbf{x}) = \frac{1}{2}\,\|\mathbf{P}\mathbf{x} - \mathbf{v}\|_2^2, \tag{40a}$$
$$g(\mathbf{x}) = \iota_{(-1,1)^N}(\mathbf{x}), \tag{40b}$$
$$h(\mathbf{L}\mathbf{x}) = \eta\|\mathbf{y}\|_1, \tag{40c}$$
$$\mathbf{L}\mathbf{x} = \mathbf{y} = \mathfrak{D}_\mathrm{z}\mathbf{x} \tag{40d}$$

where $\mathbf{L} = \mathfrak{D}_\mathrm{z}$. We then obtain the PDS steps as shown in Algorithm 5.

It is lightweight because it does not require analysis or synthesis processing within iterations, but only a combination of convolutional operations, metric projection, and soft thresholding.

Appendix E
Interference Waveform Estimation

This appendix describes a method for identifying the coherence functions in (2). The identification of the measurement process is based on thin glass substrate data, making it easier than biological tissue to reveal the impulse response as the measurement process. For the identification problem, the least-squares method with the gradient descent algorithm was used after detecting the position and slope of the glass surfaces by plane fitting. The formula for the identification is set to

$$\hat{\boldsymbol{\theta}} = \arg\min_{\boldsymbol{\theta}} E(\boldsymbol{\theta}), \tag{41a}$$
$$E(\boldsymbol{\theta}) = \frac{1}{2}\|\mathbf{P}_{\boldsymbol{\theta}}\mathbf{r}_\mathrm{g} - \mathbf{v}_\mathrm{g}\|_2^2, \tag{41b}$$
$$\hat{\mathbf{P}} = \mathbf{P}_{\hat{\boldsymbol{\theta}}}, \tag{41c}$$

where $\mathbf{r}_\mathrm{g} \in \mathbb{R}^N$ is assumed to have only two nonzero coefficients in the Z direction, $\mathbf{v}_\mathrm{g} \in \mathbb{R}^M$ denotes the observation data of the thin glass substrate, $\mathbf{P}_{\boldsymbol{\theta}} \in \mathbb{R}^{M\times N}$ is a measurement process with parameter set $\boldsymbol{\theta} = [\theta_i]_i = [\alpha_\mathrm{p}, \sigma_\mathrm{xy}, \sigma_\mathrm{z}, \omega_\mathrm{p}, b_\mathrm{p}]$, as in (2). The gradient of the error function $E(\boldsymbol{\theta})$ in (41) is derived analytically as

$$[\nabla_{\boldsymbol{\theta}}E(\boldsymbol{\theta})]_i = \left(\frac{\partial\mathbf{P}_{\boldsymbol{\theta}}}{\partial\theta_i}\mathbf{r}_\mathrm{g}\right)^\mathsf{T}(\mathbf{P}_{\boldsymbol{\theta}}\mathbf{r}_\mathrm{g} - \mathbf{v}_\mathrm{g}), \tag{42}$$

and $\boldsymbol{\theta}$ is optimized using this gradient.

Acknowledgement

The authors would like to thank the associate editor Prof. Ivan Selesnick and the anonymous reviewers for their valuable comments and suggestions to improve the quality of this paper.

References

[1] J. M. Schmitt, "Optical coherence tomography (OCT): a review," *IEEE Journal of Selected Topics in Quantum Electronics*, vol. 5, no. 4, pp. 1205–1215, Jul 1999.
[2] S. Apostolopoulos and R. Sznitman, "Efficient OCT volume reconstruction from slitlamp microscopes," *IEEE Transactions on Biomedical Engineering*, vol. 64, no. 10, pp. 2403–2410, Oct 2017.
[3] D. M. Freeman S. S. Hong, "Doppler optical coherence microscopy for studies of cochlear mechanics," *Journal of Biomedical Optics*, vol. 11, no. 5, pp. 1 – 5, 2006.
[4] S. S. Gao, R. Wang, P. D. Raphael, Y. Moayedi, A. K. Groves, J. Zuo, B. E. Applegate, and J. S. Oghalai, "Vibration of the organ of corti within the cochlear apex in mice," *Journal of Neurophysiology*, vol. 112, no. 5, pp. 1192–1204, 2014.
[5] S. S. Gao, P. D. Raphael, R. Wang, J. Park, A. Xia, B. E. Applegate, and J. S. Oghalai, "In vivo vibrometry inside the apex of the mouse cochlea using spectral domain optical coherence tomography," *Biomed. Opt. Express*, vol. 4, no. 2, pp. 230–240, Feb 2013.
[6] B. E. Applegate, R. L. Shelton, S. S. Gao, and J. S. Oghalai, "Imaging high-frequency periodic motion in the mouse ear with coherently interleaved optical coherence tomography," *Opt. Lett.*, vol. 36, no. 23, pp. 4716–4718, Dec. 2011.

[7] S. Choi, T. Watanabe, T. Suzuki, F. Nin, H. Hibino, and O. Sasaki, "Multifrequency swept common-path en-face OCT for wide-field measurement of interior surface vibrations in thick biological tissues," *Opt. Express*, vol. 23, no. 16, pp. 21078–21089, Aug. 2015.

[8] S. Choi, K. Sato, T. Ota, F. Nin, S. Muramatsu, and H. Hibino, "Multifrequency-swept optical coherence microscopy for highspeed full-field tomographic vibrometry in biological tissues," *Biomed. Opt. Express*, vol. 8, no. 2, pp. 608–621, Feb. 2017.

[9] S. Choi, F. Nin, T. Ota, K. Sato, S. Muramatsu, and H. Hibino, "In vivo tomographic visualization of intracochlear vibration using a supercontinuum multifrequency-swept optical coherence microscope," *Biomed. Opt. Express*, vol. 10, no. 7, pp. 3317–3342, July 2019.

[10] S. Muramatsu, S. Choi, and T. Kawamura, "3-D OCT data denoising with nonseparable oversampled lapped transform," in *2015 Asia-Pacific Signal and Information Processing Association Annual Summit and Conference (APSIPA)*, pp. 901–906, Dec. 2015.

[11] J. Cheng, D. Tao, Y. Quan, D. W. K. Wong, G. C. M. Cheung, M. Akiba, and J. Liu, "Speckle reduction in 3D optical coherence tomography of retina by a-scan reconstruction," *IEEE Transactions on Medical Imaging*, vol. 35, no. 10, pp. 2270–2279, Oct. 2016.

[12] L. Fang, S. Li, R. P. McNabb, Q. Nie, A. N. Kuo, C. A. Toth, J. A. Izatt, and S. Farsiu, "Fast acquisition and reconstruction of optical coherence tomography images via sparse representation," *IEEE Transactions on Medical Imaging*, vol. 32, no. 11, pp. 2034–2049, Nov. 2013.

[13] F. Zaki, Y. Wang, H. Su, X. Yuan, and X. Liu, "Noise adaptive wavelet thresholding for speckle noise removal in optical coherence tomography," *Biomedical Optics Express*, vol. 8, no. 5, 2017.

[14] M. Shamouilian and I. Selesnick, "Total variation denoising for optical coherence tomography," *2019 IEEE Signal Processing in Medicine and Biology Symposium (SPMB*, pp. 1-5, 2019.

[15] Y. Hu, J. Yang, J. Cheng, and J. Liu, "Noise Redistribution and 3D Shearlet Filtering for Speckle Reduction in Optical Coherence Tomography," in *Proceedings - International Symposium on Biomedical Imaging*, pp. 1565–1569, 2020

[16] S. Muramatsu, S. Choi, S. Ono, T. Ota, F. Nin, and H. Hibino, "OCT volumetric data restoration via prima-dual plug-and-play method," in *2018 IEEE International Conference on Acoustics, Audio and Signal Processing (ICASSP)*, pp. 801–805, Apr. 2018.

[17] S. Ono, "Primal-dual plug-and-play image restoration," *IEEE Signal Processing Letters*, vol. 24, no. 8, pp. 1108–1112, Aug. 2017.

[18] L. Condat, "A primal–dual splitting method for convex optimization involving Lipschitzian, proximable and linear composite terms," *Journal of Optimization Theory and Applications*, vol. 158, no. 2, pp. 460–479, Aug. 2013.

[19] S. Ono and I. Yamada, "Hierarchical convex optimization with primal-dual splitting," *IEEE Transactions on Signal Processing*, vol. 63, no. 2, pp. 373–388, Jan. 2015.

[20] J. Eckstein and D. P. Bertsekas, "On the Douglas—Rachford splitting method and the proximal point algorithm for maximal monotone operators," *Mathematical Programming*, vol. 55, no. 1, pp. 293–318, Apr. 1992.

[21] D. Gabay and B. Mercier, "A dual algorithm for the solution of nonlinear variational problems via finite element approximation," *Computers & Mathematics with Applications*, vol. 2, no. 1, pp. 17 – 40, 1976.

[22] R. G. Baraniuk, T. Goldstein, A. C. Sankaranarayanan, C. Studer, A. Veeraraghavan, and M. B. Wakin, "Compressive video sensing: Algorithms, architectures, and applications," *IEEE Signal Processing Magazine*, vol. 34, no. 1, pp. 52–66, Jan. 2017.

[23] G. Fujii, Y. Yoshida, S. Muramatsu, S. Ono, S. Choi, T. Ota, F. Nin, and H. Hibino, "OCT Volumetric Data Restoration with Latent Distribution of Refractive Index," in *Proceedings - International Conference on Image Processing, (ICIP)*, pp. 764–768, Sept. 2019.

[24] G. J. Tearney (Eds.) B. E. Bouma, *Handbook of optical coherence tomography*, Marcel Dekker, 2003.

[25] J. Kovačević and A. Chebira, "Life beyond bases: The advent of frames (part i)," *IEEE Signal Processing Magazine*, vol. 24, no. 4, pp. 86–104, July 2007.

[26] J. L. Starck, F. Murtagh, and J. Fadili, *Sparse Image and Signal Processing: Wavelets and Related Geometric Multiscale Analysis*, Cambridge University Press, 2015.

[27] M. Unser, "Texture classification and segmentation using wavelet frames," *IEEE Transactions on Image Processing*, vol. 4, no. 11, pp. 1549–1560, Nov. 1995.

[28] S. Muramatsu, K. Furuya, and N. Yuki, "Multidimensional nonseparable oversampled lapped transforms: Theory and design," *IEEE Transactions on Signal Processing*, vol. 65, no. 5, pp. 1251–1264, March 2017.

[29] C. Kilkenny and D. G. Altman, "Improving bioscience research reporting: ARRIVE-ing at a solution," *Laboratory Animals*, vol. 44, no. 4, pp. 377–378, 2010.

[30] M. P. Sato, T. Higuchi, F. Nin, G. Ogata, S. Sawamura, T. Yoshida, T. Ota, K. Hori, S. Komune, S. Uetsuka, S. Choi, M. Masuda, T. Watabe, S. Kanzaki, K. Ogawa, H. Inohara, S. Sakamoto, H. Takebayashi, K. Doi, K. F. Tanaka, and H. Hibino, "Hearing Loss Controlled by Optogenetic Stimulation of Nonexcitable Nonglial Cells in the Cochlea of the Inner Ear," *Frontiers in Molecular Neuroscience*, vol. 10, article 300, pp. 1–16, Sept. 2017.

Ruiki Kobayashi (S'20) received his B.E. and M.E. degrees from Niigata University, Niigata, Japan, in 2020 and 2022, respectively.

His research interests include multidimensional signal processing and image restoration.

Genki Fujii received his B.E. and M.E. degrees from Niigata University, Niigata, Japan, in 2016 and 2018, respectively. He was a short-term student at the Faculty of Engineering, Chulalongkorn University, Thailand, between September 2017 and March 2018. Since 2019, he has worked at Sony Semiconductor Solutions Corporation. His research interests were in sparsity-aware image and volumetric data restoration.

Yuta Yoshida received his B.E. and M.E. degrees from Niigata University, Niigata, Japan, in 2017 and 2019, respectively. Since 2020, he has worked at NEC Solution Inovators, Ltd. His research interests were in hardware implementation of image processing and volumetric data restoration.

Takeru Ota obtained a BSc degree in Physico-informatics at Keio University in 2009 and received an MSc degree in Physics and a PhD degree in Dentistry in 2011 and 2016, respectively, at Tohoku University. In 2016, he joined Niigata University and worked on the research of auditory physiology with optical coherence tomography and laser interferometry. He is currently an Assistant Professor at the Division of Glocal Pharmacology, Department of Pharmacology, Graduate School of Medicine, Osaka University. He is continuing the research and to try to understand the mechanic of hearing with his engineering skills.

Fumiaki Nin received his MD degrees and PhD from Kyoto Prefectural University of Medicine, Kyoto, Japan, in 2000 and 2009, respectively. From 2000 to 2005, he worked at Kyoto Prefectural University of Medicine as an otorhinolaryngologist. From 2006 to 2008, he joined the Department of Pharmacology II, Osaka University Graduate School of Medicine as a special research student. From 2010 to 2012, he was a research fellow at the Department of Sensory Neuroscience in the Rockefeller University. From 2012 to 2020, he was an assistant and associate professor in the Department of Physiology in Niigata University Graduate School of Dental and Medical Sciences. From 2020, he is a professor of the Department of Physiology in Gifu University Graduate School of Medicine. His research interests include cochlear physiology, biophysics, electrophysiology, mathematical modeling, and biomedical optics. Prof. Nin is a council member of the Physiological Society of Japan, and a member of the Japanese Pharmacological Society, the Otorhinolaryngological Society of Japan, and Japan Otological Society.

Hiroshi Hibino graduated from Osaka University Faculty of Medicine in 1994 with medical license and then received PhD degree in Medicine in 1999. After studying in Jim Hudspeth lab as a postdoc at the Rockefeller University from 1999 to 2002, he got back Osaka University and worked as an assistant professor and an associate professor for several years. In 2010, he obtained an appointment of the professor in Niigata University School of Medicine. Recently, he has moved to Osaka University Graduate School of Medicine and conducts his own group as the professor and chairman at Division of Glocal Pharmacology, Department of Pharmacology. His project is the elucidation of the mechanisms underlying the functions and pathophysiology of the cochlea.

Samuel Choi received his B.E. and M.E. degrees from Tohoku University, Sendai, Japan in 2002 and 2004, respectively. In 2007, he received his Dr. Eng. degree from Tokyo University of Agriculture and Technology (TUAT), Tokyo, Japan. From 2008 to 2009, he worked at TUAT as a JSPS International Research Fellow. In 2009, he joined Niigata University, where he is currently an associate professor in the Faculty of Engineering. His research interest includes optoelectronics, optical metrology, optical interferometry, nonlinear optics, Fourier optics, biomedical imaging, optical coherence tomography, and optical imaging system. Prof. Choi is a member of Optical Society of America, SPIE - The International Society for Optical Engineering, and Japan Society of Applied Physics. He was awarded Konica Minolta Imaging Science Award in 2015.

Shunsuke Ono received a B.E. degree in Computer Science in 2010 and M.E. and Ph.D. degrees in Communications and Computer Engineering in 2012 and 2014 from the Tokyo Institute of Technology, respectively. From April 2012 to September 2014, he was a Research Fellow (DC1) of the Japan Society for the Promotion of Science (JSPS). He is currently an Associate Professor in the Department of Computer Science, School of Computing, Tokyo Institute of Technology. From October 2016 to March 2020, he was a Researcher of Precursory Research for Embryonic Science and Technology (PRESTO), Japan Science and Technology Corporation (JST), Tokyo, Japan. His research interests include signal processing, computational imaging, hyperspectral imaging and processing, mathematical optimization, and data science. Dr. Ono received the Young Researchers' Award and the Excellent Paper Award from the IEICE in 2013 and 2014, respectively, the Outstanding Student Journal Paper Award and the Young Author Best Paper Award from the IEEE SPS Japan Chapter in 2014 and 2020, respectively, the Funai Research Award from the Funai Foundation in 2017, and the Ando Incentive Prize from the Foundation of Ando Laboratory in 2021. He has been an Associate Editor of IEEE Transactions on Signal and Information Processing Over Networks since 2019.

Shogo Muramatsu (S'93-M'98-SM'14) received his B.E. and M.E. degrees and Ph.D. from Tokyo Metropolitan University, Tokyo, Japan, in 1993, 1995, and 1998, respectively. From 1997 to 1999, he worked at Tokyo Metropolitan University. In 1999, he joined Niigata University, where he is currently a professor in the Faculty of Engineering. From 2003 to 2004, he was a visiting researcher at the University of Florence, Italy. His research interests include cyber-physical systems, multidimensional signal processing, image restoration, video analysis, and embedded vision systems. Prof. Muramatsu is a senior member of the Institute of Electronics, Information, and Communication Engineers (IEICE) of Japan and a member of the Asia-Pacific Signal and Information Processing Association (APSIPA) and the Institute of Image Information and Television Engineers (ITE) of Japan. He has been an associate editor for IEEE Transactions on Signal Processing since 2019 and was an APSIPA distinguished lecturer from 2020 to 2021.